International Journal of Mechanical Sciences 237 (2023) 107806

Contents lists available at ScienceDirect

International Journal of Mechanical Sciences

journal homepage: www.elsevier.com/locate/ijmecsci

A peridynamic elasto-plastic damage model for ion-irradiated materials

M. Nowak [a], K. Mulewska [b], A. Azarov [c], Ł. Kurpaska [b], A. Ustrzycka [a,*]

[a] Institute of Fundamental Technological Research, Polish Academy of Sciences, Pawińskiego 5b, 02-106, Warsaw, Poland
[b] NOMATEN Centre of Excellence, National Centre for Nuclear Research, ul. A. Soltana 7, 05-400 Otwock, Poland
[c] University of Oslo, Centre for Materials Science and Nanotechnology, PO Box 1048 Blindern, N-0316 Oslo, Norway

ARTICLE INFO

Keywords:
Peridynamics
Constitutive modelling
Radiation induced damage
Peridynamic porosity
Gurson yield function
Irradiation hardening
Ion irradiation
Nano-indentation test

ABSTRACT

This study presents the novel peridynamic constitutive relations formulated in order to predict the plastic deformation and damage evolution in irradiated materials. The plastic behaviour of the material in which radiation induced defects contribute to the defined peridynamic porosity is described by the Gurson–Tvergaard–Needleman (GTN) yield criterion with irradiation hardening. The definition of peridynamic porosity is proposed as a volume of discontinuities created in the volume of peridynamic particles. The new constitutive relations for irradiation hardening based on the dilatational part of elastic strain energy are formulated. The physical relevance of coupling the porosity with the nonlinear irradiation hardening is discussed. The expressions for the yield function, kinetics of evolution of radiation induced porosity, irradiation hardening and plastic flow rule are derived in terms of the peridynamics variables. The peridynamic predictions are calibrated based on the experimental data obtained during the advanced experimental campaigns dedicated to irradiated materials to verify the validity of the proposed constitutive model. Ion irradiation campaigns were carried out to mimic the effects of neutron irradiation. A series of indentation experiments were conducted to elucidate the effects of material structure modification and assess the hardening effect originating from radiation defects.

1. Introduction

In many metallic materials, high plastic deformation is always accompanied by ductile failure. The evolution of plastic strain fields in materials subjected to applied stresses that exceed their yield strength is directly related to the phenomenon of ductile damage. Plastic strain induced damage is a cause of possible failure in structural components. The reasons for failure can be multiple, fatigue damage accumulation, corrosion, the pre-existing nano-, and microscopic material imperfections often act as starting point for material failure. The assessment of damage generated in materials subjected to high neutron flux and further evolution of the defects under mechanical loads is a major challenge in technological domains connected to nuclear industries. In polycrystalline metals, nano-defects in the form of clusters of voids, clusters of interstitials, dislocation loops and helium bubbles are the main sign of irradiation damage. Radiation induced defects interact with the microstructure of the materials leading to a mechanical response characterized by radiation hardening, increased yield strengths, reduction in ductility, decreased total strain to failure and increased embrittlement as compared to the unirradiated behaviour [1–4]. The problem of the evolution of radiation-induced defects is particularly important in the new generation of nuclear reactors, particle accelerators or detectors. It is known that the components subjected to radiation demand stable mechanical, thermal and structural properties over a large temperature and neutron fluence range. Moreover, the attractiveness of nuclear power as a present and future energy source is driven by new concepts of advanced reactors that offer reliability. New concepts include more aggressive environments, higher temperatures, and greater levels of radiation damage. The material behaviour in the radiative environment plays an important role and makes the constitutive modelling of irradiation effect on mechanical properties a subject of great importance [5–7]. The nature of the radiation induced defects has a multiscale character. The radiation defects are induced by the interaction of energetic incident particles with lattice atoms. At the same time, their effects are manifested at the component (engineering) level [2]. Prediction of the multiscale damage process before failure is still a major challenge within the framework of classical mechanics. The phenomenological continuum damage mechanics (CDM) enables analysis of the damage development. Extensive studies based on the concepts of the effective stress and mechanical equivalence between the damaged and the undamaged material have been presented in the last decade's [8–13]. The micromechanical description of ductile failure in metals and alloys during plastic deformation is generally identified as the micro-voids nucleation, growth and coalescence [14–16]. The investigations of ductile failure using Gurson–Tvergaard–Needleman

* Corresponding author.
E-mail address: austrzyc@ippt.pan.pl (A. Ustrzycka).

https://doi.org/10.1016/j.ijmecsci.2022.107806
Received 23 August 2022; Received in revised form 24 September 2022; Accepted 29 September 2022
Available online 5 October 2022
0020-7403/© 2023 The Authors. Published by Elsevier Ltd. This is an open access article under the CC BY license (http://creativecommons.org/licenses/by/4.0/).

(GTN) damage model are still developed [17–19]. However, in order to recognize the physical mechanisms responsible for the behaviour of metals and achieve an effective lifetime estimation, more research on the analysis of damage initiation and evolution is needed.

Peridynamics (PD) is a novel theory proposed by Silling [20] based on integral form for the equation of motion giving the possibility to improve modelling of progressive failure in materials. Further, the theory of peridynamics enables the solution of multi-physics and multiscale problems. Due to this reason, peridynamics is often used to describe the damage in ductile materials [21–23]. Further, PD belongs to the nonlocal and meshless methods because it considers finite distance interactions among the material particles [20]. Therefor, it is well suited to problems related to crack propagation and failure [24–26]. It is worth pointing out that the classical local plasticity models are mostly unsuitable for describing size-dependent plastic flow behaviour. Due to this reason, the rapid development of nonlocal theories like gradient plasticity with the advantage of including the direct-neighbour interactions and non-neighbour interactions inside the material structure has occurred [27–30]. Nonlocal theories have been proposed in order to model inhomogeneous plastic flow. Recently, a new approach taking non-locality through fractional derivatives, which, by definition, require a certain neighbourhood to calculate their values has been proposed. Sumelka and Nowak [31] applied the fraction operator to the plastic flow rule in nonlocal anisotropic plastic model with non-normality of plastic flow and volume change caused by plastic deformation. Similar results have been obtained in [32], where the fractional nonlocal viscoplasticity model with scalar damage, interpreted as porosity, is proposed.

In order to obtain a complete description of damage evolution and the final failure many numerical models use the so-called eXtended Finite Element Method (X-FEM). Crété et al. [33] retained the X-FEM method to describe the engineering materials' failure resulting from void initiation and growth. Although the X-FEM has found many practical applications, there are still open questions related to the choice of reliable fracture criteria and the initial size of the finite element mesh. In the meshless method the mesh is not required. Therefore, the damage and resulting discontinuities can be introduced more naturally. The detailed comparison of X-FEM and peridynamics methods is presented in [34], highlighting their advantages and disadvantages. Peridynamics gives new perspectives for solving physically-based multiscale problems and new possibilities for modelling of the evaluation of damage generated in solids [35]. For modelling the evolution of material damage in peridynamics, the failure criterion based on the critical value of bond relative elongation for breakage was formulated by Silling and Askari [21]. The criterion fulfilment determines the irreversible break and the bond no longer sustains a force. Such an approach to the failure problem can be successfully applied to brittle materials, hence, the name of the material model is Prototype Microelastic Brittle (PMB). It is worth pointing out, that even though the material is isotropic at the beginning of the process, the history dependent failure of bonds leads to anisotropy in successive deformation steps. Mandeci and Oterkus [36] proposed a new formulation of damage modelling for plastic deformation. They utilized the classical Huber–Mises–Hencky (HMH) yield condition with isotropic hardening in the state-based peridynamic method. In a similar way, a classical approach to plasticity in terms of peridynamics is presented by Pashazad and Kharazi [37]. The modified form of kinematic hardening and the mixed of isotropic and kinematic hardening is proposed. For this reason, the proposed plastic model has been used to predict the behaviour of the material subjected to cyclic loadings.

Along with the faster development of peridynamics, the question arose whether the classical continuum constitutive models can be used directly in peridynamics. Silling [38] proposed the so-called "PD corresponds material models" which provide a way to convert an already developed continuum model in peridynamics framework. These models use a shape tensor to convert peridynamics variables into stress and strain measures. Tupek et al. [39] used the modified Johnson–Cook constitutive model with damage evolution to analyse the failure in the Taylor impact test which involves large deformation. Recently, Hu et al. [40] utilized the classic GTN constitutive model in peridynamics to study the ductile fracture in steel plate. The developed model allowed the correct description of necking phenomena and damage propagation during plastic deformation. More and more classical continuum materials models are incorporated in the peridynamics framework, even though such an approach has some limitations and drawbacks associated with instabilities [41]. For this reason, the model presented in this work is based on the pure definition of vector states of peridynamics theory. Such an approach allows the direct definition of the new physical quantities and, in an efficient way, builds the new variables into the constitutive model.

In this paper the peridynamic elasto-plastic damage model based on the Gurson–Tvergaard–Needleman (GTN) yield condition for ion-irradiated materials is proposed. The PD damage constitutive model operating on the forces, deformation states and the elastic strain energy decomposed into dilatational and distortional parts with a specific focus on irradiation hardening is presented. The damage variable is defined at the level of the peridynamic particle and characterized by a reduction of effective force transmission capacity caused by the coupling effect of the damage evolution and the bond elongation increment. The driving force for porosity evolution is the rate of dilatation part of the plastic stretch.

The paper is structured as follows, Section 2 introduces the fully coupled pressure-dependent damage constitutive model. The constitutive relations are derived in terms of the horizon, force density and peridynamic strain energy density. In order to validate numerical simulations the original experiments were carried out. The results of the ion irradiation campaign are presented in Section 3. For the thin ion-irradiated layers the nano-indentation technique has been adopted in order to quantify the damage evolution reflected by the load–displacement curves. In Section 4, the computational studies are carried out and discussed.

2. Pressure-dependent damage constitutive model

The present Section is dedicated to a definition of peridynamic constitutive relations. Moreover, the concept of the peridynamic elasto-plastic damage model is proposed. Section 2.1 is partially dedicated to a brief review of peridynamic theory (Eqs. (1)–(15)) formulated by Madenci and Oterkus [36]. Moreover, in this Section new peridynamic constitutive relations are formulated: the Gurson–Tvergaard–Needleman (GTN) yield function in terms of peridynamics variables (Eq. (11)), equivalent stress $q_{(k)}$ (Eq. (17)) and pressure $p_{(k)}$ (Eq. (18)). The peridynamic porosity parameter is defined in Section 2.2. The irradiation induced hardening is defined in Section 2.3. The peridynamic elasto-plastic model accounting the irradiation effects is formulated in Section 2.4. In Section 2.5 the numerical solution procedure for the elasto-plastic constitutive model is explained.

2.1. Peridynamics elasto-plastic relations

Peridynamics is a nonlocal theory, which for a given material point takes into account the through-bonds interactions between all material points located in its close neighbourhood. The size of the neighbourhood is controlled by the horizon h, which can be considered as the length scale parameter. The equation of motion for state-based peridynamics [38] is expressed in the form

$$\rho(\mathbf{x})\ddot{\mathbf{u}}(\mathbf{x},t) = \int_H \left[\mathbf{t}(\mathbf{u}-\mathbf{u}', \mathbf{x}-\mathbf{x}', t) - \mathbf{t}'(\mathbf{u}'-\mathbf{u}, \mathbf{x}'-\mathbf{x}, t)\right] dH + \mathbf{b}(\mathbf{x},t) \quad (1)$$

where each material point is identified by $\mathbf{x}$, ρ is the density, $\mathbf{u}$ denotes the displacement vector, $\mathbf{b}$ is the body force vector, $\mathbf{t}$ is the force state and H defines a family region of neighbouring materials points. The

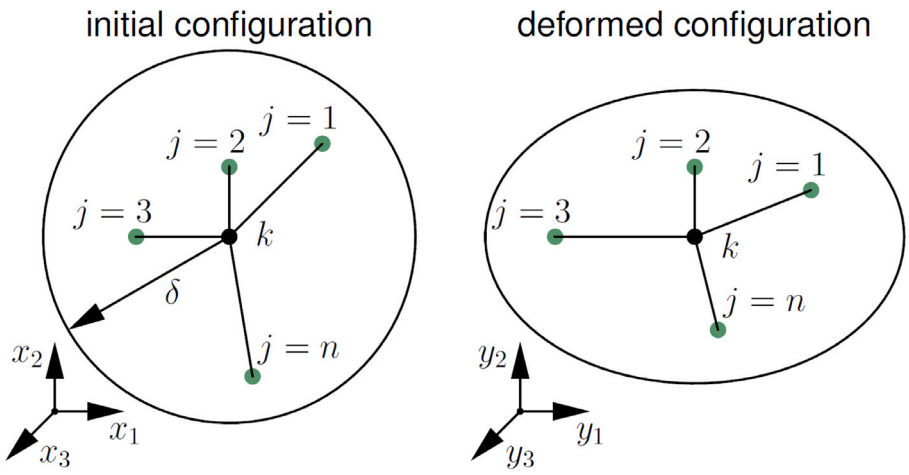

Fig. 1. Peridynamics neighbourhood of the material point k before and after applied deformation.

superscript prim denotes the quantities that are determined for the neighbouring point. As shown in [36], the equation of motion (1) can be expressed in discretized form as

$$\rho_k \ddot{\mathbf{u}}_k = \sum_{j=1}^{n} \left[\mathbf{t}_{(k)(j)}(\mathbf{u}_{(j)} - \mathbf{u}_{(k)}, \mathbf{x}_{(j)} - \mathbf{x}_{(k)}, t) \right. \\ \left. -\mathbf{t}_{(j)(k)}(\mathbf{u}_{(k)} - \mathbf{u}_{(j)}, \mathbf{x}_{(k)} - \mathbf{x}_{(j)}, t) \right] V_{(j)} + \mathbf{b}_{(k)} \tag{2}$$

where lower subscript (k) defines the material point and n is the number of materials points located in family region. $V_{(j)}$ denotes the volume associated with the point (j). The family of material point before and after deformation is shown in Fig. 1.

During deformation, any two material points k and j can change their initial position and move to the new location. If the displacement vectors of these points are different, the bond between them stretches locally and the material can change its original shape (Fig. 1). The stretch, $s_{(k)(j)}$, between material points k and j is defined in the following form

$$s_{(k)(j)} = \frac{|\mathbf{y}_{(j)} - \mathbf{y}_{(k)}| - |\mathbf{x}_{(j)} - \mathbf{x}_{(k)}|}{|\mathbf{x}_{(j)} - \mathbf{x}_{(k)}|} \tag{3}$$

where $\mathbf{y}$ denotes position vector in the current configuration. Next, the peridynamic strain energy density at a material point k can be written as

$$W_{(k)} = (a_\kappa - a_\mu)\theta^2_{(k)} + b\delta \sum_{i=1}^{N} s^2_{(k)(j)} |\mathbf{x}_{(j)} - \mathbf{x}_{(k)}| V_{(j)} \tag{4}$$

where $\theta_{(k)}$ is the dilatation term defined as

$$\theta_{(k)} = d\delta \sum_{i=1}^{N} s^2_{(k)(j)} |\mathbf{x}_{(j)} - \mathbf{x}_{(k)}| V_{(j)} \tag{5}$$

The material parameters: $a_\kappa = \frac{1}{2}\kappa$, $a_\mu = \frac{5}{6}\mu$, $b = \frac{15\mu}{2\pi\delta^5}$ and $d = \frac{9}{4\pi\delta^4}$ are expressed in terms of peridynamics horizon δ where μ denotes the shear modulus and κ is the bulk modulus. Applying Eq. (3), the dilatation takes the form

$$\theta_{(k)} = d\delta \sum_{i=1}^{N} s_{(k)(j)} \Lambda_{(k)(j)} V_{(j)} \tag{6}$$

where $\Lambda_{(k)(j)}$ is defined in the following form

$$\Lambda_{(k)(j)} = \frac{\mathbf{y}_{(j)} - \mathbf{y}_{(k)}}{|\mathbf{y}_{(j)} - \mathbf{y}_{(k)}|} \frac{\mathbf{x}_{(j)} - \mathbf{x}_{(k)}}{|\mathbf{x}_{(j)} - \mathbf{x}_{(k)}|} \tag{7}$$

Following the concept presented in [36], the elastic strain energy can be decomposed into dilatational and distortional parts as

$$W_{(k)} = W^\kappa_{(k)} + W^\mu_{(k)}, \tag{8}$$

where

$$W^\kappa_{(k)} = a_\kappa \theta^2_{(k)} \tag{9}$$

and

$$W^\mu_{(k)} = b \sum_{j=1}^{N} \delta s^2_{(k)(j)} |\mathbf{x}_{(j)} - \mathbf{x}_{(k)}| V_{(j)} - a_\mu \theta^2_{(k)} \tag{10}$$

The force density vector expressed by the bond stretch can be obtained by differentiating the elastic energy (Eq. (4)) with respect to the current bond length $|\mathbf{y}_{(j)} - \mathbf{y}_{(k)}|$

$$t_{(k)(j)} = (a_\kappa - a_\mu) 2\delta d \frac{\Lambda_{(k)(j)}}{|\mathbf{x}_{(j)} - \mathbf{x}_{(k)}|} \theta_{(k)} + 2\delta b s_{(k)(j)} \tag{11}$$

The force density vector (its magnitude) can also be decomposed into distortional $t^\mu_{(k)(j)}$ and dilatational $t^\kappa_{(k)(j)}$ terms as

$$t_{(k)(j)} = t^\mu_{(k)(j)} + t^\kappa_{(k)(j)} \tag{12}$$

Both terms of the force density vector can be expressed as a function of stretch $s_{(k)(j)}$ and dilatation $\theta_{(k)}$ in the following form

$$t^\kappa_{(k)(j)} = \frac{2\delta a_\kappa d \Lambda_{(k)(j)}}{|\mathbf{x}_{(j)} - \mathbf{x}_{(k)}|} \theta_{(k)} \tag{13}$$

and

$$t^\mu_{(k)(j)} = 2\delta b s_{(k)(j)} - \frac{2\delta a_\mu d}{|\mathbf{x}_{(j)} - \mathbf{x}_{(k)}|} \Lambda_{(k)(j)} \theta_{(k)} \tag{14}$$

The decomposition of Hook's law into two orthogonal states allows to define distortional part of elastic energy in the following form

$$W^\mu_{(k)} = b \sum_{j=1}^{N} \delta \left(\frac{1}{2\delta b} t^\mu_{(k)(j)} + a_\mu \frac{d}{b} \frac{\Lambda_{(k)(j)}}{|\mathbf{x}_{(j)} - \mathbf{x}_{(k)}|} \theta_{(k)} \right)^2 |\mathbf{x}_{(j)} - \mathbf{x}_{(k)}| V_{(j)} - a_\mu \theta^2_{(k)} \tag{15}$$

The plastic behaviour of the material is described by the Gurson–Tvergaard–Needleman (GTN) yield function formulated in terms of peridynamics variables as follows

$$F_{(k)} = \left(\frac{q_{(k)}}{\sigma^y_{(k)}} \right)^2 + 2q_1 f_{(k)} \cosh \left(\frac{3q_2 p_{(k)}}{2\sigma^y_{(k)}} \right) - (1 + q_3 f^2_{(k)}) \tag{16}$$

where $\sigma^y_{(k)}$ corresponds to the current yield stress, $f_{(k)}$ is the porosity at a material point $\mathbf{x}_{(k)}$.

The equivalent stress $q_{(k)}$ and pressure $p_{(k)}$ at a material point $\mathbf{x}_{(k)}$ can be expressed in term of the dilatational and distortional parts of the elastic energies, respectively, as follows

$$q_{(k)} = \sqrt{6\mu W^\mu_{(k)}} \tag{17}$$

and

$$p_{(k)} = \sqrt{2\kappa W^{\kappa}_{(k)}} = \sqrt{2\kappa a_{\kappa}}\theta_{(k)} \tag{18}$$

The total stretch can be decomposed into elastic and plastic part in the following form

$$s_{(k)(j)} = s^{e}_{(k)(j)} + s^{p}_{(k)(j)} \tag{19}$$

Similarly, the total dilatation can be split into elastic and plastic part as

$$\theta_{(k)} = \theta^{e}_{(k)} + \theta^{p}_{(k)} \tag{20}$$

It is worth pointing out, that in the case of the pressure dependent material model (GTN model) the plastic part of the dilatation can naturally reach non-zero values $\theta^{p}_{(k)} \neq 0$. Also, if the deformation of the material is in the elastic range, $F_{(k)} < 0$, the force density vector is computed according to Eq. (11). Otherwise, the following form of plastic flow rule is adopted

$$\Delta s^{p}_{(k)(j)} = \frac{1}{V_j} C_{(k)} \frac{\partial F_{(k)}(p_{(k)}, q_{(k)})}{\partial t_{(k)(j)}} \tag{21}$$

where $C_{(k)}$ is a positive proportionality constant. For the pressure-sensitive yield function, it is convenient to express the flow rule (Eq. (21)) in the following form

$$\Delta s^{p}_{(k)(j)} = \frac{1}{V_{(j)}} C_{(k)} \left(\frac{\partial F_{(k)}(p_{(k)}, q_{(k)})}{\partial p_{(k)}} \frac{\partial p_{(k)}}{\partial t_{(k)(j)}} + \frac{\partial F_{(k)}(p_{(k)}, q_{(k)})}{\partial q_{(k)}} \frac{\partial q_{(k)}}{\partial t_{(k)(j)}} \right) \tag{22}$$

New variables are defined

$$\Delta s^{pp}_{(k)} = C_{(k)} \frac{\partial F_{(k)}(p_{(k)}, q_{(k)})}{\partial p_{(k)}} \tag{23}$$

and

$$\Delta s^{pq}_{(k)} = C_{(k)} \frac{\partial F_{(k)}(p_{(k)}, q_{(k)})}{\partial q_{(k)}} \tag{24}$$

where $\Delta s^{pq}_{(k)}$ and $\Delta s^{pp}_{(k)}$ denote the increments of plastic bound stretch. The above Eqs. (23), (24) represent the distortion and dilatation part of plastic deformation, respectively. The incremental plastic stretch can be rewritten in the form

$$\Delta s^{p}_{(k)(j)} = \frac{1}{V_{(j)}} \left[\Delta s^{pp}_{(k)} \frac{\partial p_{(k)}}{\partial t_{(k)(j)}} + \Delta s^{pq}_{(k)} \frac{\partial q_{(k)}}{\partial t_{(k)(j)}} \right] \tag{25}$$

Eliminating $C_{(k)}$ from Eqs. (23) and (24) leads to

$$\Delta s^{pp}_{(k)} \frac{\partial F_{(k)}}{\partial q_{(k)}} - \Delta s^{pq}_{(k)} \frac{\partial F_{(k)}}{\partial p_{(k)}} = 0 \tag{26}$$

2.2. Peridynamic porosity

The damage evolution in materials described by peridynamics theory means the progressive physical process which leads to the growth of voids in the volume of the peridynamic particles. In the present paper, damage is defined as the nano/micro volumes of discontinuities created in the volume of the peridynamic particles. Consequently, the damage evolution leads to the weakening of the bonds as a result of the reduction of particle volume and the accumulation of forces in the neighbourhood of defected volume. The local concentration of internal forces results from the damage evolution and heterogeneous deformation of the material. Finally, the critical value of the damage parameter for the single peridynamic particle leads to the breaking of bonds connected with this particle and consequently to material failure. It is worth pointing out, that all stages of damage evolution may be studied using the proposed damage variables in the framework of peridynamics theory.

Peridynamic porosity $f_{(k)}(x,t)$ is defined as a ratio between the integrated volume of voids and the total volume of peridynamic particle.

$$f_{(k)}(x_{(k)}, t) = \frac{V^{f}_{(k)}}{V_{(k)}} \tag{27}$$

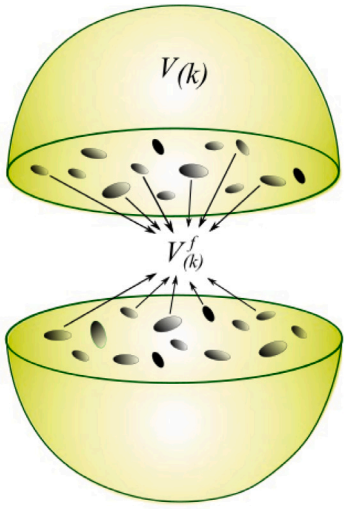

Fig. 2. Integrated volume of voids $V^{f}_{(k)}$ within the peridynamic particle volume $V_{(k)}$.

where $x_{(k)}$ denotes the material point, $V_{(k)}$ is the peridynamic volume of particle and $V^{f}_{(k)}$ is the effective volume of the all voids which lie in $V_{(k)}$. A damaged peridynamic particle is shown in Fig. 2.

The value of the peridynamic porosity parameter is limited in the range $0 \leq f_{(k)}(x_{(k)}, t) \leq 1$, where $f_{(k)} = 0$ denotes undamaged peridynamic particle and $f_{(k)} = 1$ denotes the fully decohesion of the peridynamic particle. In fact, the failure occurs through a process of instability for the critical level of porosity parameter reaching the value of $f^{cr} = 0.3$. It is assumed, that such value is enough to the initiation of crack propagation [42]. The evolution law for porosity is derived from the expression for porosity in the following form

$$f_{(k)} = \frac{V_{(k)} - V_{m(k)}}{V_{(k)}} = 1 - \frac{V_{m(k)}}{V_{(k)}} \tag{28}$$

where $V_{m(k)}$ is the matrix of the peridynamic particle.

As a result of the differentiation of Eq. (28) with respect to time the relationship for rate of the void volume fraction is obtained

$$\dot{f}_{(k)} = \frac{V_{m(k)}}{V_{(k)}} \frac{\dot{V}_{(k)}}{V_{(k)}} = (1 - f_{(k)}) \frac{\dot{V}_{(k)}}{V_{(k)}} \tag{29}$$

where $V_{m(k)}$ is the matrix of the peridynamic particle.

In the light of the above, the kinetic law for porosity is expressed in the following form

$$\dot{f}_{(k)} = (1 - f_{(k)}) \dot{s}^{pp}_{(k)} \tag{30}$$

where $\dot{s}^{pp}_{(k)}$ is the rate of plastic stretch which corresponds to dilatation state. The evolution of peridynamic porosity leads to the plastic enlargement of cavities inside the volume of material particles. In particular, the characteristic features of the proposed definition of porosity in peridynamics are summarized in the following way:

- Damage is incorporated in the peridynamics theory at the level of the peridynamic particle
- Physical meaning of damage is understood as the increase of microvoids within the peridynamic particle at the expense of the particle volume
- Increase of microdefects leads to weakening of the bonds
- Damage localization and evolution occur as a natural outgrowth of the equation of motion and constitutive models
- Peridynamic damage of material is characterized by the reduction of effective force transmission capacity caused by the coupling effect of the damage evolution and the bond elongation increment

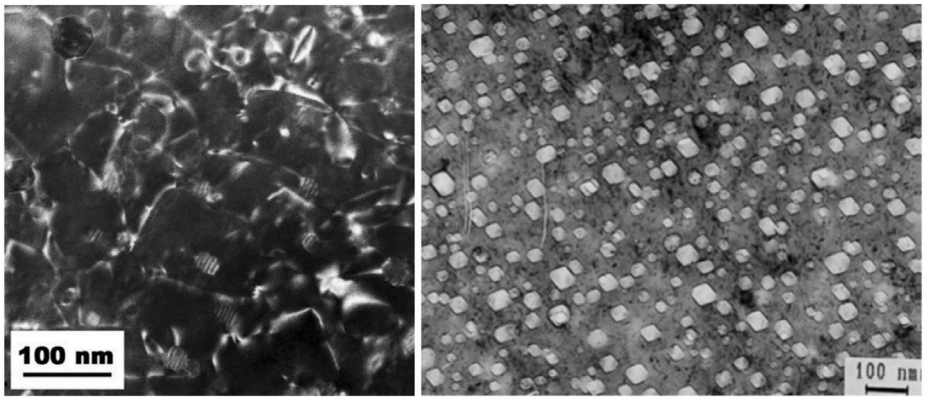

Fig. 3. (a) TEM image showing dislocation loops, precipitates and voids in irradiated HT9 ferritic/martensitic steel at 155 *dpa* [46] (b) voids observed in irradiated austenitic stainless steel EI-847 at 73 *dpa* [47].

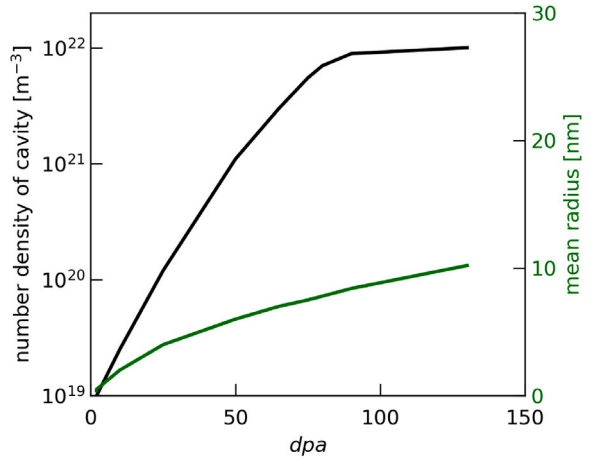

Fig. 4. Density of cavity and average cluster size as a function of irradiation dose, based on [48].

Thus, the proposed formulation of porosity remains classical and is based on Gurson's porosity plasticity model [14,43,44]. The complex nature of radiation defects is close to porosity because of formation of clusters of vacancies and cavities. The origin of initial porosity (radiation induced damage or micro-damage of mechanical origin) in the material is not significant but it is an important shaping parameter of the global material response under multi-axial stress state. Therefore, the proposed peridynamic damage model based on the evolution of porosity appears to be suitable for irradiated materials [2,45]. Radiation induced changes in the form of spherical voids in austenitic stainless steel are shown in Fig. 3. The shape of radiation induced clusters in the form of spherical voids is shown in the TEM micrograph.

For this reason, the models describing the porosity evolution appear most suitable in the case of the irradiated materials [1,2,45]. One of the most important mechanisms of failure in irradiated materials is the growth and evolution of voids. The consequences of irradiation of component's structure are increased hardening, ductility reduction and embrittlement. The density of cavities (empty voids and voids filled with helium) and average cluster size as a function of irradiation dose are shown in Fig. 4.

Radiation induced porosity $f^{irr}_{0(k)}$ is based on the mean value of radius $r^c_{(k)}$ and density $q^c_{(k)}$ of vacancy clusters. The clusters of radiation defects of the size of several nanometers are qualified as spherical voids

$$f^{irr}_{0(k)} = q^c_{(k)} \frac{4}{3}\pi \left(r^c_{(k)}\right)^3 \tag{31}$$

The measure of radiation induced defects in the solid is *dpa* unit which expresses the number of atoms displaced from their initial displacements [49]. As shown in Fig. 4 *dpa* reflects the formation of particular types of defects including clusters of nanovoids that can be recalculated to the peridynamic porosity parameter. Clusters of nanovoids are the major damage structures in materials subjected to strong neutron irradiation. Spherical nanovoids are randomly distributed in the spatial domain. As a result, irradiated materials, including steels become highly porous (Fig. 3). Thus, nanovoids are observed at higher doses of neutron irradiation. For this reason, the present paper assumed that *dpa* reflects mainly the formation of vacancy clusters, and can be converted to the peridynamic porosity parameter. It is worth underlining, that in the irradiated solids, as a result of the reaction between fast neutrons and metal nuclei, the effect of generation and growth of helium bubbles takes place. In this case, the helium porosity with different internal pressure in bubbles is created. To account for, all the other forms of defects like dislocation loops, clusters of interstitial atoms and cavities filled with impurities, the kinetics of evolution of these defects under mechanical loads must be established.

For the relationship of cluster density of cavities $q^c_{(k)}$ and the average cluster radius $r^c_{(k)}$ as a function of dpa, the power law is employed

$$q^c_{(k)} = c_q (dpa_{(k)})^{n_q}, \quad r^c_{(k)} = c_r (dpa_{(k)})^{n_r} \tag{32}$$

where c_q, c_r, n_q, n_r are the material parameters determined using experimental results obtained by Courcelle et al. [48]. Referring to Eq. (31) the porosity parameter can be expressed as a function of radiation damage measure (dpa)

$$f^{irr}_{0(k)} = \frac{4}{3}\pi c_q c_r^3 \left(dpa_{(k)}\right)^{3n_r+n_q} \tag{33}$$

It has been assumed, that the failure of irradiated material occurs as soon as the maximum porosity parameter characterizes peridynamic particle reaches the value of $f^{cr} = 0.3$. In order to predict the material failure, the critical value of total porosity parameter $f^{cr}_{(k)}$ is adopted. The critical value of porosity parameter also means the breaking all peridynamic bonds connected with the corresponding peridynamic particle. It results from the reduction of effective force transmission capacity caused by the coupling effect of the damage evolution and the bond elongation increment.

2.3. Irradiation hardening

In order to capture the isotropic hardening behaviour in PD elasto-plastic damage model it is assumed that the current yield stress is a function of equivalent plastic stretch $\bar{s}_{(k)}$, radiation damage levels dpa and current porosity $f_{(k)}$

$$\sigma^y_{(k)} = \sigma^y_{(k)}(\bar{s}_{(k)}, dpa_{(k)}, f_{(k)}) \tag{34}$$

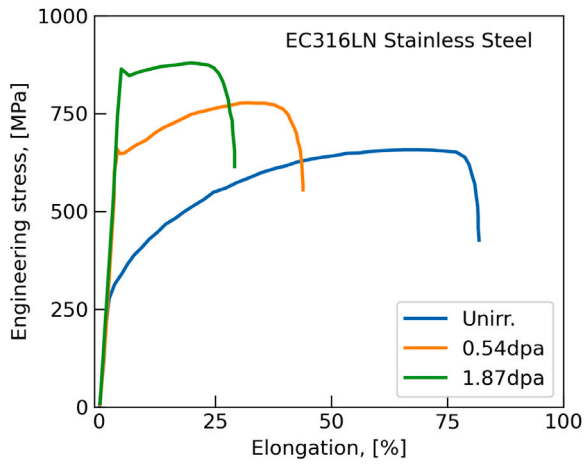

Fig. 5. Engineering stress–strain curves of EC316LN stainless steel after irradiation to labelled doses in spallation environments [51].

The equivalent plastic strain is obtained by assuming that the microscopic plastic power of the porous solid varies according to the equivalent plastic work expression

$$\bar{s}_{(k)} = A_0 \frac{p_{(k)} \Delta s^{pp}_{(k)} + q_{(k)} \Delta s^{pq}_{(k)}}{(1-f)\sigma^{y}_{(k)}} \tag{35}$$

The additional parameter A_0 was determined by Madenci and Oterkus [36] by comparison of the equivalent plastic stretch during uniaxial tension using peridynamics and classical continuum theory. Thus, for 3D case the parameter A_0 is defined as

$$A_0 = \frac{\sqrt{5}}{\sqrt{\pi b \delta^5}} \tag{36}$$

Interaction of dislocation generated during deformation with radiation induced defects in the form of randomly distributed spherical voids leads to changes in mechanical properties of the material, such as increase in yield stress, embrittlement and hardness [1,3,50]. Randomly distributed voids and helium bubbles become barriers to undisturbed dislocations motion and plastic flow. The influence of irradiation-induced defects on strain hardening and softening is analysed.

The Kocks–Mecking type hardening model [52] is the main way to obtain a physically based description of irradiation hardening law. The yield function expressed by the components that contribute to the irradiation hardening takes the form

$$\sigma^{y}_{(k)} = h_d \alpha \mu \sqrt{\bar{s}_{(k)}} + \sigma^{y0_{irr}}_{(k)} - h_a \mu \bar{s}_{(k)} \sqrt{f_{(k)}} + \sigma_a exp\left(-\frac{\bar{s}_{(k)}}{s_0}\right) \tag{37}$$

where h_d is a proportional factor, h_a is a parameter with opposite signs controlling the annihilation of dislocations, α denotes the Taylor strengthening coefficient and μ denotes the shear modulus.

For non-irradiated materials, a strain hardening regime can be observed, which is related to the interaction among dislocations (compare Fig. 5). The first term in Eq. (37) $\left(h_d \alpha \mu \sqrt{\bar{s}}\right)$ describes the strain hardening mechanism. Dislocation motion is impeded by the presence of obstacles in the form of forest dislocations acting as random obstacles

The increase of the initial yield point $\sigma^{y0^{irr}}_{(k)}$ resulting directly from the increase of irradiation dose (dpa) is expressed in the following form

$$\sigma^{y0irr}_{(k)} = \sigma^{y0}_{(k)} + B_2 \sigma^{y0}_{(k)} \sqrt{dpa} \tag{38}$$

Moreover, the expression in Eq. (38) is closely related to the initial yield strength of the non-irradiated material $\sigma^{y0}_{(k)}$ [51,53].

The dislocations dynamics is controlled by the annihilation process reducing the dislocation density during the plastic deformation. Moreover, during the interaction of dislocation with voids (weak precipitate), the dislocation can separate and dissociate into partial dislocations [54,55]. The third part $\left(-h_a \mu \bar{s}_{(k)} \sqrt{f_{(k)}}\right)$ describes the mechanisms responsible for softening.

The unpinning term $\left(\sigma_a exp\left(-\frac{\bar{s}_{(k)}}{s_0}\right)\right)$ is introduced based on the observation that larger radiation obstacles require higher stress to unpin [50,54] where σ_a denotes the reference stress for dislocation unpinning

$$\sigma_a\left(f_{(k)}, \bar{s}_{(k)}\right) = B_0 \alpha \mu \bar{s}_{(k)} \sqrt{\left| f_{(k)}\left(s^{pp}_{(k)}\right) - f^{0}_{(k)} \right|} \tag{39}$$

$f^{0}_{(k)}$ is the initial porosity resulting from radiation and s_0 denotes a coefficient to adjust the avalanche speed after unpinning the dislocations.

The modelling of irradiation hardening in metals for advanced nuclear reactors is based on the mechanisms of irradiation hardening due to the various irradiation-produced defects. Irradiation-induced defects produced in radiation cascades act as barriers to dislocation gliding. This leads to an increase in the overall yield stress of the material. It is assumed in the present paper, that the peridynamic porosity is the main source of radiation hardening. The hardening model includes mechanisms of blocking dislocations at radiation-induced defects and the annihilation of dislocations with opposite Burger's vector or as a result of interaction with voids. Also, the general behaviour of the irradiation hardening model shows that as the radiation-induced porosity increases, the initial yield point increases.

2.4. Model summary

The proposed pressure-dependent damage material model with irradiated isotropic hardening consists of the following system of equations (see Box I)

The advanced constitutive model consider fully coupled dissipative phenomena in the irradiated material. The peridynamic elasto-plastic model includes coupling the volumetric damage parameter with the yield function. This formulation is kept based on the Gurson model. In the original Gurson model, the void coupled yield function is derived from the void deformation behaviour in a matrix material [56]. In addition, peridynamic damage of material is characterized by the reduction of effective force transmission capacity caused by the coupling effect of the damage evolution and the bond elongation increment. Moreover, the hardening and softening rules are introduced to control the evolution of the yield function. The nonlinear irradiation hardening and softening are coupled with the porosity variation. This coupling effect results in an overall hardening and softening behaviour, owing to the combined effects of both damage and plasticity.

The nonlinear system of Eqs. (40) is solved using the iterative Newton method. A series of numerical tests demonstrate the efficiency of the well-calibrated physically based constitutive model. Details of the iterative solution can be found in the Appendix.

2.5. Numerical solution procedure for elastic–plastic constitutive model

A numerical procedure of the developed peridynamics model can be implemented in the following steps listed below for a given particle (k). The goal of the algorithm is to provide the basic equations to calculate the peridynamics variables in the $(n+1)$ calculation step based on the known value from the previous one (n). Moreover, the goal of the described algorithm is to show the step by step instruction for evaluation of the force density vector ${}^{n+1}t_{(k)(j)}$ based on the known value of the total stretch ${}^{n+1}s_{(k)(j)}$.

1. Save the data from the previous calculation step n

$${}^{n}s_{(k)(j)}, \quad {}^{n}s^{e}_{(k)(j)}, \quad {}^{n}s^{p}_{(k)(j)}, \quad {}^{n}\bar{s}_{(k)}, \quad {}^{n}f_{(k)}, \quad {}^{n}\sigma^{y}_{(k)}$$

$$
\begin{aligned}
t_{(k)(j)} &= (a_\kappa - a_\mu)2\delta d\,\frac{\Lambda_{(k)(j)}}{|\mathbf{x}_{(j)}-\mathbf{x}_{(k)}|}\theta_{(k)} + 2\delta b s_{(k)(j)} && \text{- isotropic Hooke's law if} \quad F_{(k)} < 0\\
F_{(k)} &= \left(\frac{q_{(k)}}{\sigma^y_{(k)}}\right)^2 + 2q_1 f_{(k)}\cosh\left(\frac{3q_2 p_{(k)}}{2\sigma^y_{(k)}}\right) - (1+q_3 f^2_{(k)}) = 0 && \text{- yield function}\\
\Delta s^{pp}_{(k)}\frac{\partial F_{(k)}}{\partial q_{(k)}} &- \Delta s^{pq}_{(k)}\frac{\partial F_{(k)}}{\partial p_{(k)}} = 0 && \text{- plastic flow rule}\\
\sigma^y_{(k)} &= h_d\alpha\mu\sqrt{\bar{s}_{(k)}} + \sigma^{y0}_{(k)irr} - h_a\mu\bar{s}_{(k)}\sqrt{f_{(k)}} + \sigma_a exp\left(-\frac{\bar{s}_{(k)}}{s_0}\right) && \text{- irradiated hardening/softening}\\
\Delta f_{(k)} &= (1-f_{(k)})\Delta s^{pp}_{(k)} && \text{- kinetic law of porosity}
\end{aligned}
\tag{40}
$$

Box I.

2. Get the value of the current bound stretch ${}^{n+1}s_{(k)(j)}$ in the family bonds of point (k).
3. Calculate trial elastic stretch ${}^{n+1}s^t_{(k)(j)}$ and trial elastic dilatation ${}^{n+1}\theta^t_{(k)}$ as

$${}^{n+1}s^t_{(k)(j)} = {}^{n+1}s_{(k)(j)} - {}^{n}s^p_{(k)(j)}, \quad {}^{n+1}\theta^t_{(k)} = \sum_{j=1}^{N}\left({}^{n+1}s^t_{(k)(j)}\right)\Lambda_{(k)(j)}V_{(j)}$$

4. Calculate the trial force density as

$${}^{n+1}t^t_{(k)(j)} = \frac{2hd}{|\mathbf{x}_{(j)}-\mathbf{x}_{(k)}|}(a_\kappa - a_\mu)\Lambda_{(k)(j)}\left({}^{n+1}\theta^t_{(k)}\right) + 2hb\left({}^{n+1}s^t_{(k)(j)}\right)$$

5. Determine the trial dilatational and distortional parts of the strain energy density as

$${}^{n+1}W^\kappa_{(k)} = a_\kappa\left({}^{n+1}\theta^t_{(k)}\right)^2, \quad {}^{n+1}W^\mu_{(k)} = \sum_{j=1}^{N}\left({}^{n+1}s^t_{(k)(j)}\right)|\mathbf{x}_{(j)}-\mathbf{x}_{(k)}|V_{(j)}$$

6. Calculate trial hydrostatic stress ${}^{n+1}p^t_{(k)}$ and equivalent HMH stress ${}^{n+1}q^t_{(k)}$ as

$${}^{n+1}p^t_{(k)} = \sqrt{2Ka_\kappa}\left({}^{n+1}\theta^t_{(k)}\right), \quad {}^{n+1}q^t_{(k)} = \sqrt{6G\left({}^{n+1}W^\mu_{(k)}\right)}$$

7. Compute the value of the GTN yield function based on the trial state using Eq. (16)

$${}^{n+1}F_{(k)} = {}^{n+1}F_{(k)}\left({}^{n+1}q^t_{(k)}, {}^{n+1}p^t_{(k)}, {}^{n}f_{(k)}\right)$$

8. Check if trail calculation step is elastic

$${}^{n+1}F_{(k)} < 0$$

9. If step is elastic, set

$${}^{n+1}\Delta s^p_{(k)(j)} = 0$$

and go to step 13, otherwise go to next calculation step.
10. Apply Newton iterative method to find unknowns variables ${}^{n+1}\Delta s^{pp}_{(k)(j)}$ and ${}^{n+1}\Delta s^{pq}_{(k)(j)}$.
    (a) Assume initial values of the unknowns

$${}^{n+1}\Delta s^{pp}_{(k)(j)} = 0, \quad {}^{n+1}\Delta s^{pq}_{(k)(j)} = 0$$

    (b) Check convergence

$$|F_{(k)}| < tol, \qquad \left|{}^{n+1}\Delta s^{pp}_{(k)(j)}\frac{\partial F_{(k)}}{\partial q_{(k)}} - {}^{n+1}\Delta s^{pq}_{(k)(j)}\Delta s^{pq}_{(k)}\frac{\partial F_{(k)}}{\partial p_{(k)}}\right| < tol$$

    (c) If assumed tolerance (tol) is obtained go to step 12, otherwise go to next Newton step.
    (d) Compute jacobian matrix and solve linear system of equations for ${}^{n+1}d\Delta s^{pp}_{(k)(j)}$ and ${}^{n+1}d\Delta s^{pq}_{(k)(j)}$ according to the equations given in Appendix.
    (e) Update unknowns variables

$${}^{n+1}\Delta s^{pp}_{(k)(j)} = {}^{n+1}\Delta s^{pp}_{(k)(j)} + {}^{n+1}d\Delta s^{pp}_{(k)(j)}, \quad {}^{n+1}\Delta s^{pq}_{(k)(j)} = {}^{n+1}\Delta s^{pq}_{(k)(j)} + {}^{n+1}d\Delta s^{pq}_{(k)(j)}$$

11. Update porosity

$${}^{n+1}f_{(k)} = {}^{n}f_{(k)} + A_0(1-{}^{n}f_{(k)})\left({}^{n+1}\Delta s^{pp}_{(k)(j)}\right)$$

12. Compute the increment of plastic stretch according to Eq. (25)

$${}^{n+1}\Delta s^p_{(k)(j)} = \frac{1}{V_{(j)}}\left({}^{n+1}\Delta s^{pp}_{(k)(j)}\frac{\partial p_{(k)}}{\partial t_{(k)(j)}} + {}^{n+1}\Delta s^{pq}_{(k)(j)}\frac{\partial q_{(k)}}{\partial t_{(k)(j)}}\right)$$

13. Compute the plastic and elastic stretch

$${}^{n+1}s^p_{(k)(j)} = {}^{n}s^p_{(k)(j)} + {}^{n+1}\Delta s^p_{(k)(j)}, \quad {}^{n+1}s^e_{(k)(j)} = {}^{n+1}s_{(k)(j)} - {}^{n+1}s^p_{(k)(j)}$$

14. Compute the elastic dilatation

$${}^{n+1}\theta^e_{(k)} = {}^{n+1}\theta^t_{(k)} - {}^{n+1}\Delta\theta^p_{(k)}$$

15. Using the Hooke's law compute force density vector based on the elastic stretch and elastic dilatation

$${}^{n+1}t_{(k)(j)} = \frac{2hd}{|\mathbf{x}_{(j)}-\mathbf{x}_{(k)}|}(a_\kappa - a_\mu)\Lambda_{(k)(j)}\left({}^{n+1}\theta^e_{(k)}\right) + 2hb\left({}^{n+1}s^e_{(k)(j)}\right)$$

16. Go to the first calculation step.

3. Experiments

Experimental characterization of initiation and evolution of nano/micro damage under mechanical loads in the irradiated materials is rare in the literature. This Section is dedicated to presenting two experimental campaigns dedicated to irradiated materials. The two experimental campaigns consist of: (1) ion irradiation in a wide range of damage levels expressed in terms of displacement per atom dpa and (2) nanoindenation tests on irradiated specimens.

3.1. Ion irradiation

As an alternative to neutron irradiation, ion irradiation has become the most widely applied method to achieve radiation damage corresponding to high neutron doses. To reach that high displacement damage level, the ion irradiation method can be applicable in a relatively short time without the samples becoming radioactive. Ion irradiation belongs to the methods where the defect formation can be controlled with high accuracy (including concentration and depth distribution) and allows to obtain materials having a wide range of damage levels, usually expressed in dpa scale (displacements per atom) [49]. Ion irradiation can generate the same various defects as neutron irradiation, such as Frankel pairs, interstitials, vacancies, clusters of voids and dislocation loops. The austenitic stainless steel 310S is proposed for this analysis due to its promising thermo-mechanical properties. This kind of steel is an excellent candidate for environmentally extreme applications such as new nuclear energy systems due to

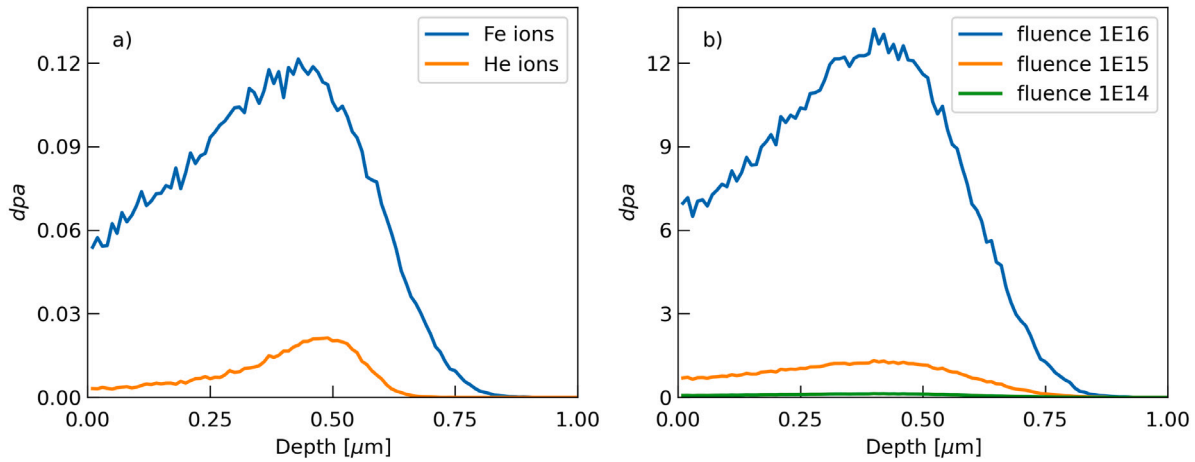

Fig. 6. Simulated irradiation damage (in *dpa*) as a function of target depth for (a) 1.5 MeV Fe ions and 160 keV He ions (b) 1.5 MeV Ni ions at the fluence of 1E14, 1E15 and 1E16 ions/cm^{-2}.

Table 1
Ion-irradiation campaign.

Ion	Fluence (ions/cm^2)	Energy	*dpa*	Porosity
Ni	1E14	1.5 MeV	0.12	4E–8
Ni	1E15	1.5 MeV	1.32	1E–5
Ni	1E16	1.5 MeV	13.22	2E–3
Fe	1E14	1.5 MeV	0.12	4E–8
He	1E15	1.0 MeV	0.02	7E–10
Fe and He	1E14 and 1E15	1.5 MeV and 160 keV	0.14	6E–8

its good corrosion resistance, high strength, and ductility. Furthermore, the amount of carbon is limited, reducing the risk of embrittlement. As-polished specimens of stainless steel 310S were irradiated at room temperature with 1.5 MeV Ni, 1.5 MeV Fe ions, and 1 MeV He ions. Fluences of these irradiations were 1E14, 1E15 and 1E16 ions/cm^{-2} for Ni, 1E14 ions/cm^{-2} for Fe and 1E15 ions/cm^{-2} for He. These conditions corresponded to the radiation-damage generation from 0.02 to 13.22 *dpa* (displacement per atom; [49]) and were calculated using SRIM software (The Stopping and Range of Ions in Matter) [57]. Described irradiation conditions also resulted in modification approx. 0.8 μm for Fe and Ni. Profiles of irradiation damage (in *dpa*) as a function of target depth for 1.5 MeV Fe ions and 160 keV He ions and for Ni ions at the fluence of 1E14, 1E15 and 1E16 ions/cm2 is shown in Fig. 6. In order to best simulate the effect of neutron irradiation one rectangular sample was submitted to sequential dual-beam ion irradiation. The parameters of ion implantation (energy) were again determined by using SRIM code [57]. In order to maximize material damage at similar depths, the energy of He + and Fe + ions were set as 160 keV and 1.5 MeV, respectively. The implantation with He-ions contributes to the creation of helium bubbles. Fluences of these irradiations were 1E14 ions/cm^{-2} and 1E15 ions/cm^2, respectively for He and Fe. These parameters corresponded to modification of ≈ 800 nm thick layer. However, the highest damage level occurs at a depth of about 500 nm, see Fig. 6. During implantation the ion beam current was limited to about 0.1 μA cm^{-2} to avoid significant heating of the samples. The temperature of the specimens was controlled continuously using a thermocouple and the irradiations were performed in the normal direction relative to the surface of the specimens. Detail description of the irradiation campaign is presented in Table 1.

Both single and double ion implantation campaigns were carried out using 3SDH-2 1.0 MV NEC Pelletron Tandem accelerator.

3.2. Nanoindentation tests

Modified layers induced by ion-irradiation are usually thin, approximately 0.1–3 μm. The depth of this modification depends on the ion energy and atomic weight of the implanted element. As a rule of thumb, higher energy results in more profound material modification, while heavier elements penetrate smaller depths of the material than light atoms (e.g., He). Generation of the irradiated layer with low thickness requires the use of nano/micro indentation technique to measure their mechanical properties. In this work, the classical nanoindentation tests using the Berkovich-shaped indenter were performed. The experimental set-up of the indentation tests is shown in Fig. 7. Fig. 7(A) shows the indenter system and the holder with a mounted tested specimen, while Fig. 7(B) depicts a snapshot of the ongoing indentation test. Fig. 7(C) shows the sample surface after indentation. One can observe a series of indents with a distance of 20 μm from each other. Fig. 7(D) shows an SEM image of the indent with the developed characteristic slip planes on each side of the indented wall-side.

Each specimen has been tested at least 10 times. In order to prevent creep of the specimen, the maximum load was kept for 1 s (up to 4.5 mN) or 2 s (up to 10 mN), while the load/unload cycle took 3 s and 2 s for loads 0.25–0.5 mN, 5 s and 3 s for loads 0.75–4.5 mN, and 10 s and 5 s for loads 5–10 mN, respectively. To prevent the interference of the imprints and their stress/strain fields, the distance of 20 μm between the indentation spots was kept. In order to measure the mechanical properties of the ion-irradiated layers, it should considered that the plastic zone's volume developed under the indenter tip is approximately 10 times thicker than the maximum indentation depth. The tests performed with 1 mN loads up to ≈ 100 nm indentation depth corresponds to this proportion and allow conclude that the recorded information comes from the irradiated region. Fig. 8 presents the indentation curves recorded for the virgin austenitic stainless steels 310S and after irradiation using Fe, Ni, and He ions. It is known that the radiation-induced defects developed during the ion-irradiation process emulate neutron damage and act as obstacles to the dislocation movement during plastic deformation. This leads to the material hardening. The currently presented results are coherent with the physical approach. The results show that the irradiation-induced hardening of the material occurs in the examined zone. This is manifested as the hardness increase with the irradiation dose (see Fig. 9).

The object of the experimental analysis was to establish the basic mechanical properties, such as the hardness of the irradiated steel as a function of the irradiation dose. The irradiated samples were tested within the wide load range from 0.25 to 10 mN. The maximum load corresponded to the range of 400 nm penetration depth. The hardness variation deduced from the load–displacement (L–D) curves as a function of indentation contact depth is shown in Fig. 9 for different values of *dpa*. The hardness increases with increasing irradiation dose (*dpa*). The evolution of the mechanical properties of ion-irradiated materials is the obvious consequence of radiation damage created in the material.

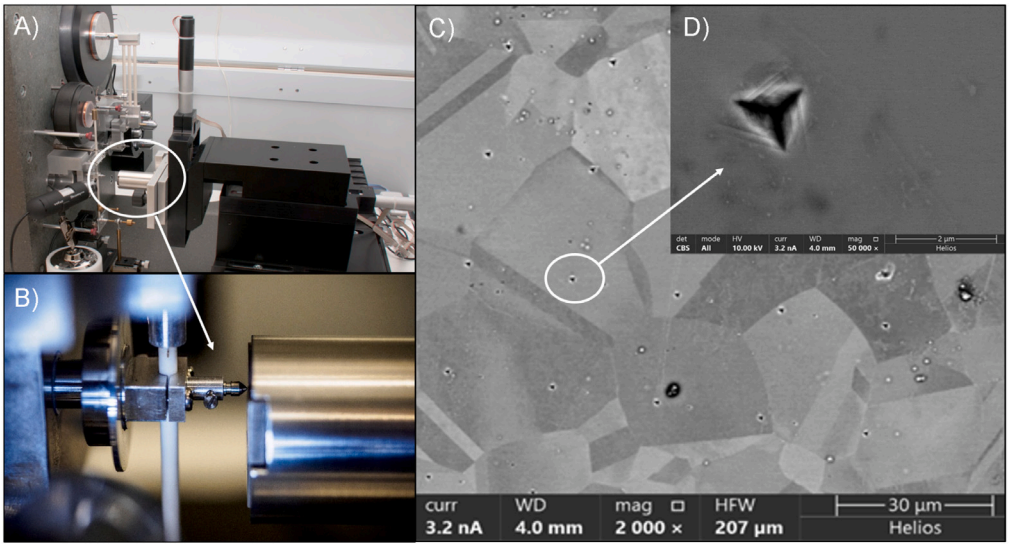

Fig. 7. (A) indenter system provided by MicroMaterials Ltd. (B) snapshot of the indentation test (C) SEM image of the 310S sample surface after indentation with 5 mN load and (D) SEM image of the indent with visible characteristic slip planes developed during material deformation while loading.

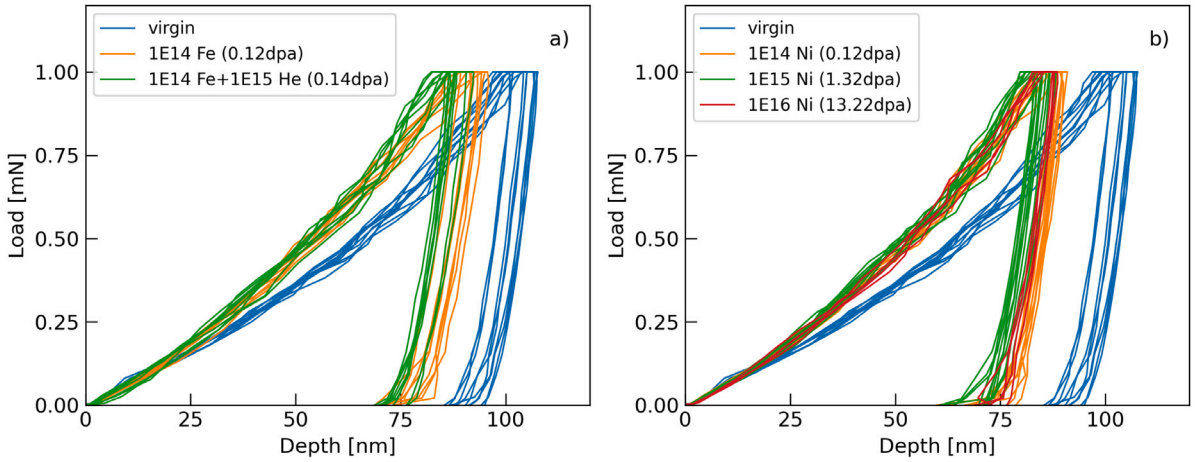

Fig. 8. Load–displacement curves on (a) virgin; Fe ion-irradiated 310SS specimen up to 0.12 *dpa*; and Fe+ He ion-irradiated 310SS specimen up to 0.14 *dpa*; (b) virgin and Ni ion-irradiated 310SS specimen for three value of irradiation dose 0.12 *dpa*, 1.32 *dpa* and 13.22 *dpa*.

On the other hand, the hardness decreases with increasing indentation depth due to the indentation size effect. Moreover, a sudden decrease in the measured hardness at the early stages of the nanoindentation process (around 80 nm indentation depth) is observed. This results from a faster accumulation rate of geometrically necessary dislocations (GNDs).

4. Results and discussion

The problem of radiation induced defects requires deep analysis from experimental, theoretical and numerical points of view. The peridynamic elasto-plastic model accounting for the irradiation effects and radiation-induced porosity is formulated in Section 2. The proposed model can be applied to study the mechanical effects of radiation damage in austenitic stainless steels and polycrystal metals or alloys used as structural materials in a reactor environment, detectors at a particle accelerator and plasma devices. Different from the phenomenological continuum damage mechanics developed by Lemaitre and Chaboche [11,16], the peridynamics theory is adopted here to solve the problem with complex boundary and loading conditions, flux of high energy particles and various mechanical loading. The proposed constitutive model in Section 2.4 has been implemented in the peridynamics numerical code using the C programming language. After implementing the relevant irradiation hardening terms, the full coupled model was applied to comprehensively study the evolution of radiation induced damage and irradiation hardening. Such a novel peridynamic approach is verified by the corresponding experimental data. The numerical simulations are performed for the different radiation induced porosity levels. The influence of different types of hardening mechanisms of porous materials on yield stress and strain hardening is shown in Section 4.1. The character of predicted by numerical model (Fig. 12) and experimental (Fig. 5) stress–strain curves for irradiated materials are compared. In Section 4.2 peridynamics model for the contact between indenter and irradiated specimen is formulated based on [21]. Finally, in Section 4.3 the numerical results are validated through the experimental measurement to verify the accuracy of the peridynamics model.

4.1. Prediction of irradiation hardening during tensile deformation

Peridynamic simulations of the tensile tests were performed on unit cube element, Fig. 10(a). The location of the analysed point is marked in Fig. 10(b). The cube specimen of the size 10 µm × 10 µm × 10 µm is

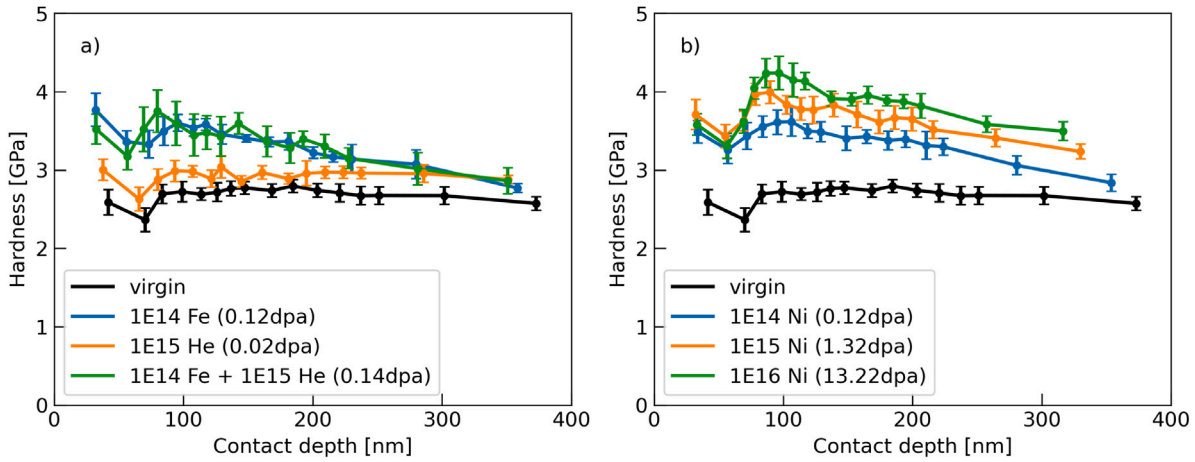

Fig. 9. Hardness variation as a function of contact depth for 310SS irradiated with (a) Fe and Fe+ He ions and (b) Ni ions.

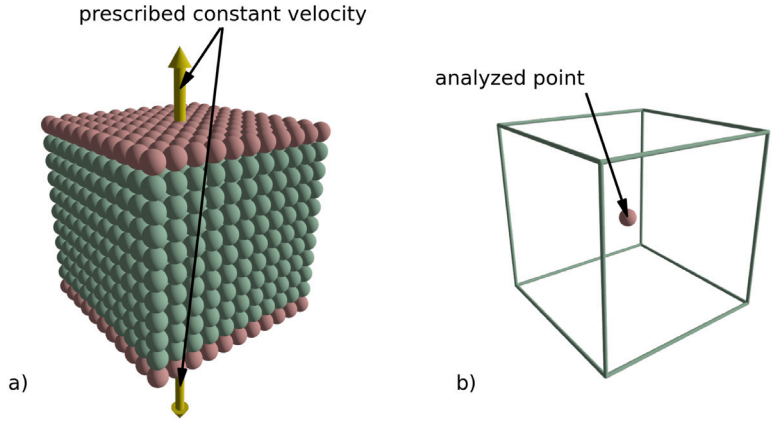

Fig. 10. (a) Schematic of the initial configuration of the peridynamics particles with marked boundary conditions for the peridynamic simulations of tensile tests (b) location of the analysed peridynamics particle.

Table 2
Parameters for the peridynamics damage plasticity model.

E [GPa]	μ [GPa]	ρ [kg/m^3]	σ_{y0} [MPa]	q_1 [–]	q_2 [–]	q_3 [–]	B_2 [–]	B_0 [–]
200	80	7800	200	1.1	1.1	2.0	3	1
h_d [–]	h_a [–]	c_q [cm^{-3}]	c_r [cm^{-3}]	n_q [–]	n_r [–]	s_0 [–]	α [–]	
0.05	3.0	1e19	5e−09	0.8	0.5	5e−1	0.3	

divided into three regions to consider boundary conditions. The prescribed vertical velocity vector was applied to the top and the bottom surface of the cube. The velocity magnitude was equal to 10 μm/s For a horizon size of $h = 3.03\Delta x$, the system has 1331 peridynamic particles and 58 147 bounds. The number of bounds associated with particles in the centre of the unit cube is 175. All material parameters used in the simulations are summarized in Table 2.

For the irradiation hardening model formulated in Section 2.3, the critical stress is decomposed into components related to the specific microstructure features of 310S namely the increase of the initial yield point associated with the increase of irradiation dose (dpa). Moreover, isotropic hardening describes the forest hardening due to the dislocation network. On the other hand, porosity-based softening is related to dislocation annihilation and separation efficiency during plastic deformation. In addition, the irradiation hardening is associated with forcing the dislocations to bow out by the radiation defects. Evolution of the stress–strain curves with selected (a) isotropic hardening, (b) porosity-based softening (c) irradiation hardening is demonstrated in Fig. 11.

Peridynamic simulations were used to examine the various hardening processes of porous materials (for different dpa levels). In the case of irradiated material the initial yield stress naturally depends on the dpa level, which defines the initial state of the material's microstructure (compare with Fig. 5). Three main features were reported: isotropic hardening, porosity-based softening and irradiation hardening. In Fig. 11(a), the simulated curves show typical work hardening plastic behaviour of materials in uniaxial tension. The strain hardening strongly depends on the increase of the dislocations concentration and is independent of porosity evolution during plastic deformation. The other hardening feature caused by the reduction in dislocation density is shown in Fig. 11(b). The dislocations annihilation rate affects the flow stress, especially at rather large strains. As a consequence, the annihilation term leads to a significant softening effect. In addition, the softening effect is enhanced with the increase of porosity due to the interaction of dislocations with voids and separating them into partial dislocations. It is worth pointing out that, the impact of defect annihilation on the macroscopic behaviour is much more pronounced at high doses of dpa. The fast decrease in the stress at the end of the simulated curves leads to the necking and failure of the material. The irradiation

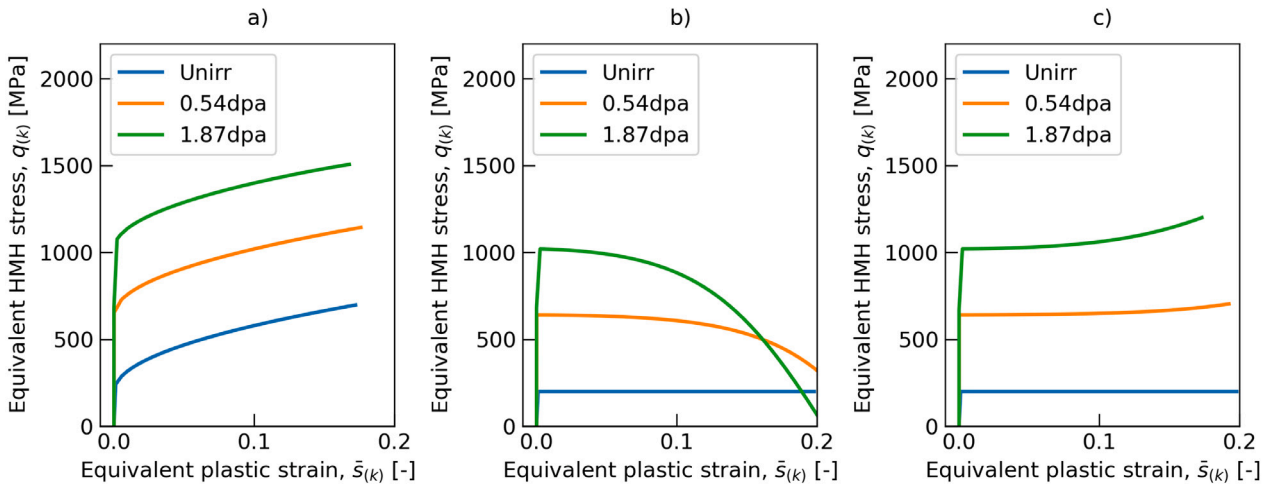

Fig. 11. Evolution of the equivalent HMH stress as a function of equivalent plastic strain with selected (a) isotropic hardening (b) porosity-based softening (c) irradiation hardening for different initial level of irradiation.

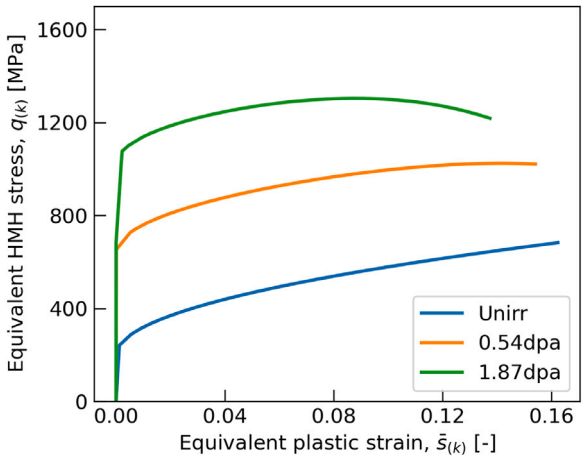

Fig. 12. Prediction of the proposed constitutive model for the uniaxial tension test with different initial level of irradiation.

hardening is observed in Fig. 11(c). This phenomenon corresponds to the blocking mechanism of the uniform motion of dislocation after encountering local obstacles, such as radiation defects. The dislocation can be unpinned by increasing the stress on the dislocation. Higher stresses are required to be able to unpin the dislocations from the local obstacles that force dislocations bowing. To summarize, prediction of the proposed elasto-plastic constitutive model with hardening-softening behaviour (Eqs. (40)) for the uniaxial tension tests is shown in Fig. 12. It is worth underlining, that the irradiation of materials leads to drastic modifications of mechanical properties: increases the yield strength, increases hardness and reduces the ductility.

The character of predicted (Fig. 12) and experimental curves (Fig. 5) for the 0.54 and 1.87 dpa doses is preserved. The proposed model is sensitive to changes of the initial yield stress with increasing dose of radiation. In addition, the constitutive model reflects well the coupling relationship between irradiation hardening resulting from blocking dislocations on radiation defects and softening connected with annihilation of radiation-induced dislocation loops. These results suggest that the proposed constitutive model is suitable for describing irradiated materials.

4.2. Peridynamics model of indentation test

The indentation test is defined as a contact problem between the indenter and the irradiated specimen, Fig. 13. Berkovic indenter is modelled as a rigid body. The geometry of the indenter consists of a set of particles with an average nearest neighbour distance equal to 50 nm forming the contact surface. The irradiated material in the form of a cube has dimensions $1600 \times 1600 \times 1600$ nm. The cube's grid step Δx is equal to 50 nm. The presented model consists of 15 625 particles and 827 267 bounds. The peridynamics horizon is assumed as $3.03 \times \Delta x$ corresponds to 175 bounds per one particle. The reaction force is calculated as a weighted sum of force density vectors $t_{(k)(j)}$ multiplied by the volume of the particles $V_{(k)}$ and projected to the direction of the indenter movement ($[0, 1, 0]$ in this case). The influence of the boundary effects resulting from a non-local approach was ignored in the simulation since a large volume of material is considered. In such a case, the boundary effects do not significantly affect the obtained results.

Based on experimental results described in Section 3, the displacement-time curves have been extracted and used as prescribed displacement of the indenter, Fig. 14. Two polynomials approximate the obtained curves: quadratic (loading stage) and linear (unloading stage). The unknown coefficient of these polynomials has been found using the least squares method.

During the indentation process, contact forces occur between the upper surface of the box and the indenter. The contact of the rigid indenter with irradiated material is modelled through short range contact forces [21]. By definition, the contact force is zero if the distance between particles (k) and (j) is greater than $d_{(k)(j)}$ (short-range interaction distance)

$$d_{(k)(j)} = min\{0.9\|x_k - x_j\|, 1.35(r_k + r_j)\} \tag{41}$$

where r is the node radius of given particle (k) or (j). It is assumed that the node radius is constant for all particles and it is equal to $\frac{1}{2}\Delta x$. Therefore, the $d_{(k)(j)}$ distance remains constant throughout the analysis. If the interaction distance between two particles is lower than $d_{(k)(j)}$, the contact force is computed using the following formula

$$F_{(k)(j)} = \frac{c_s}{\delta}\left(\|y_{(k)} - y_{(j)}\| - d_{(k)(j)}\right) V_{(k)} \frac{y_{(k)} - y_{(j)}}{\|y_{(k)} - y_{(j)}\|}, \quad c_s = 15\frac{18\kappa}{\pi\delta^4} \tag{42}$$

A bottom surface of the cube is fixed during the loading and unloading stage. All displacement components of the particles located on this surface are set to zero. Four remaining side surfaces are treated as a free surfaces. The developed material model was applied to study the material's behaviour during plastic deformation. The entire cube is assumed to made of the same homogeneous material.

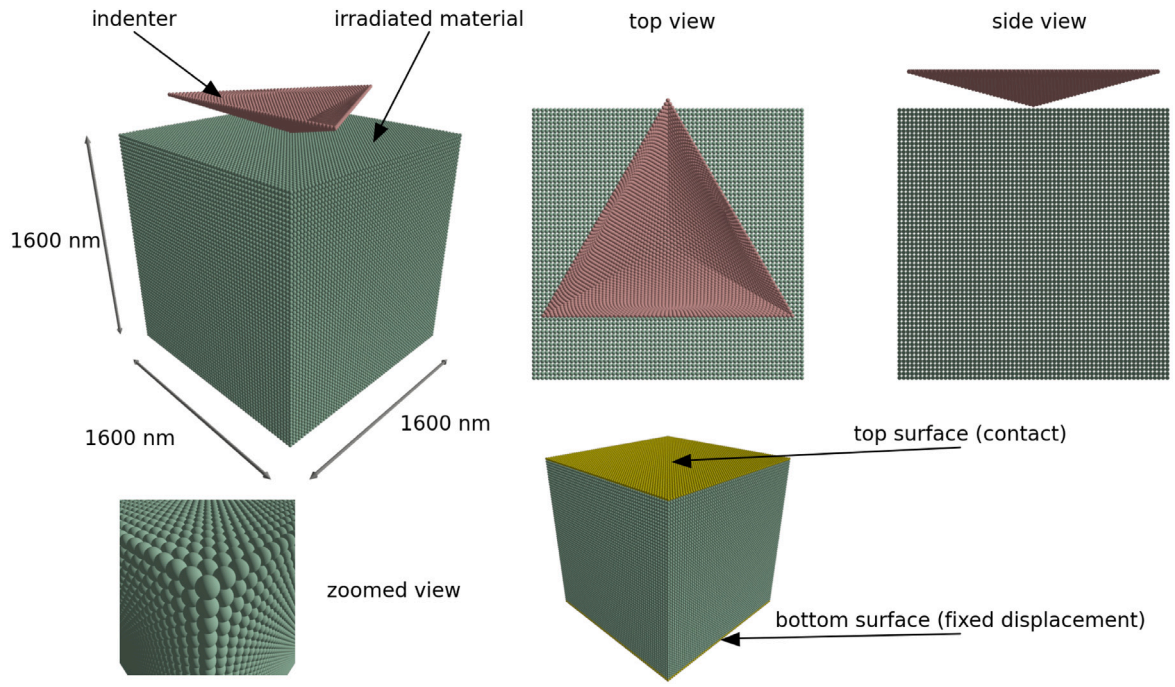

Fig. 13. Discretized peridynamics model of indentation test.

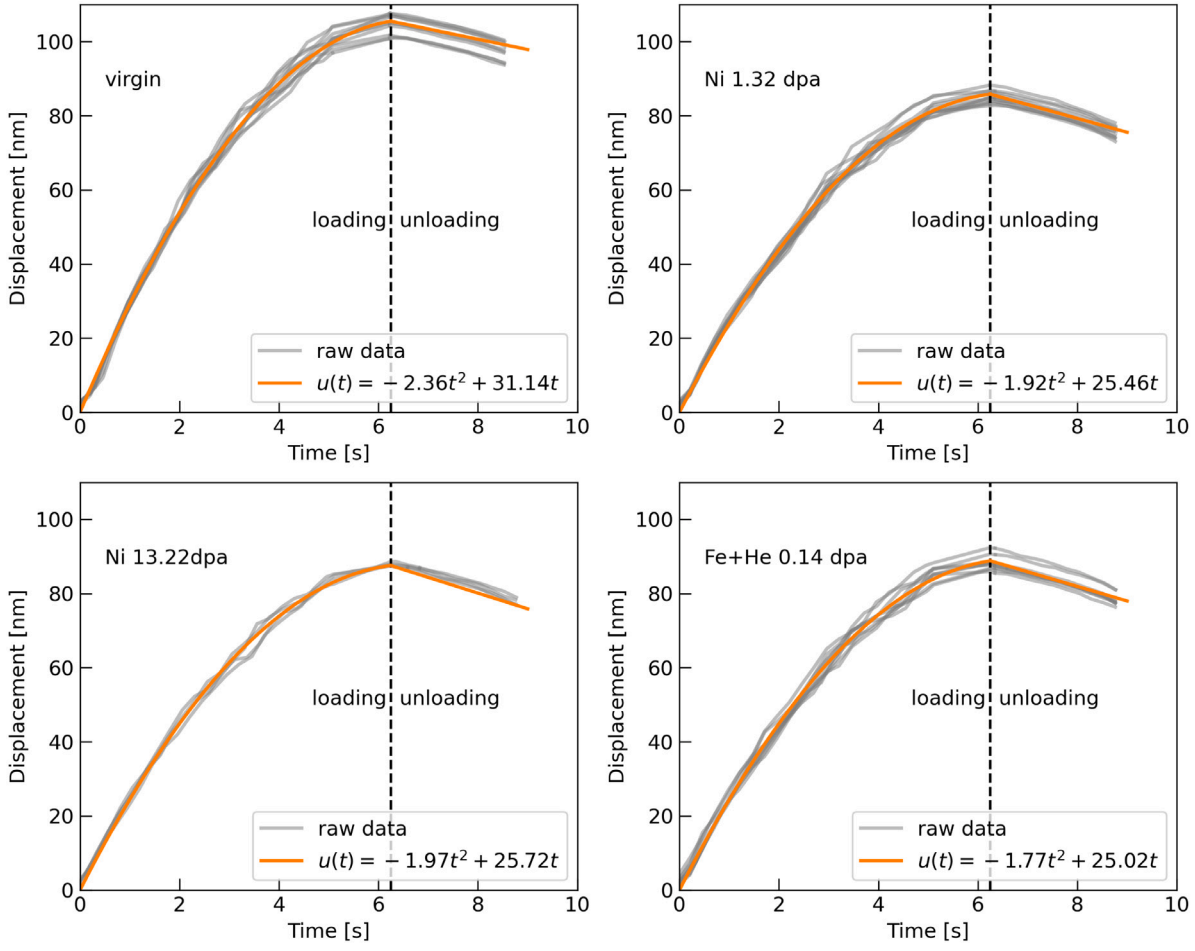

Fig. 14. Fitted analytical curves for displacement history of the indenter.

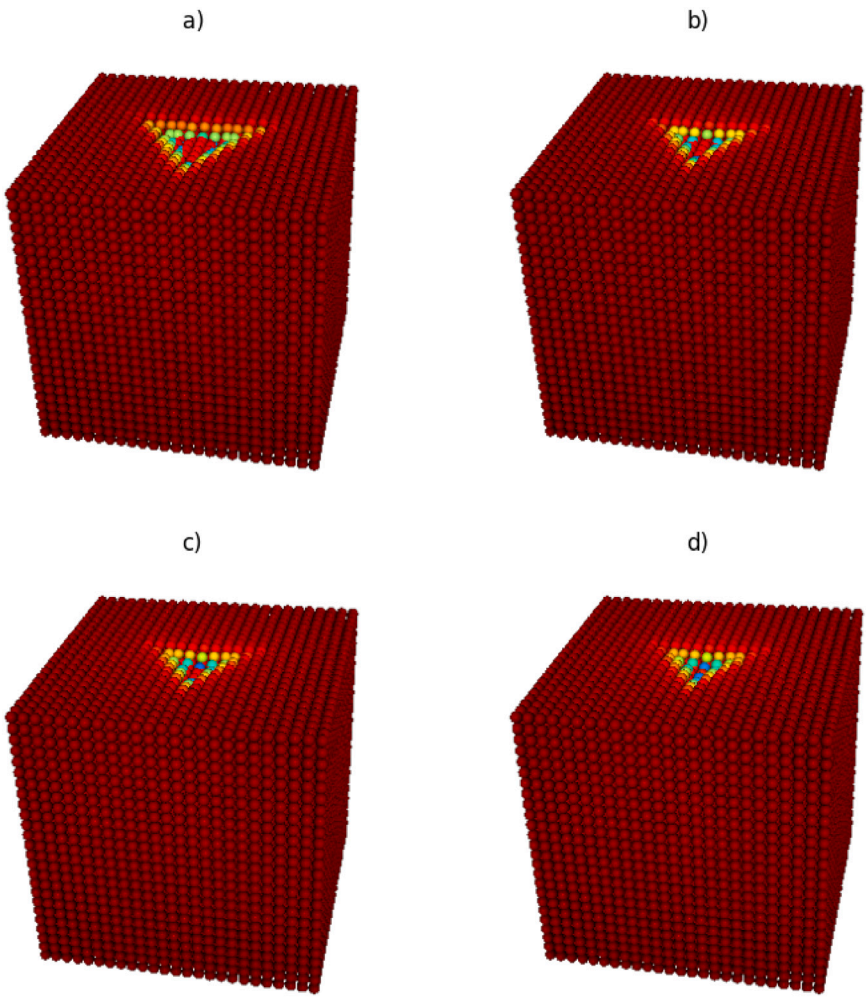

Fig. 15. Deformed configurations at the maximum indentation depth for (a) unirr (b) irr1, (c) irr2 and (d) irr3.

Table 3
Summary of selected experimental cases for numerical simulations.

No.	name	dpa	Indentation depth [nm]
unirr	Virgin	0	94.87
irr1	Fe+He 0.14	0.14	75.38
irr2	Ni 1.32	1.32	77.11
irr3	Ni 13.22	13.22	79.39

4.3. Numerical simulations

The numerical simulations for selected cases (Table 3) have been performed and validated by experiments. The four experimental cases are selected so as to represent a wide range of radiation induced damage level. As a reference to the irradiated materials, the unirradiated material is analysed. In other cases, different values of dpa are directly connected with the initial radiation induced porosity of the samples.

The results of the numerical simulations in the form of the deformed configurations of the materials at the maximum indentation depth are shown in Fig. 15. The effect of radiation porosity on the elasto-plastic behaviour of austenitic stainless steel 310S is shown. The indenter contact zone is clearly visible for all studied cases.

A dislocation nucleation mechanism, propagation behaviour and interaction of dislocations with nano/microdefects play a critical role in the plastic behaviour of irradiated and non-irradiated materials. The force applied to a structure causing deformation is proportional to the contact zone size. The reduced increase of plastic zone size for the irradiated materials results of radiation induced defects acting as obstacles to deformation in the irradiated material. Radiation induced porosity causes higher stress concentrations leading to the increase of embrittlement and in the consequence the brittle failure of the matrix material.

The comparison between the numerical and the experimental force–displacement curves for virgin material and the material irradiated to different values of dpa are presented in Fig. 16. Generally, the simulations have been limited to the indentation depth of some 80 nm, which corresponds to 10 of the maximum ion-irradiation depth. The maximum load reaches some 1 mN.

The hardening slope results both from the defined irradiated hardening and from the geometric nonlinearity, resulting from the shape of the indenter and the increasing contact surface with the material. The predictions of the proposed constitutive model are in good agreement with the experimental data.

In a similar way, the distribution of equivalent HMH stress is shown in Fig. 17. At the nanoscale, the dominant mechanism of plastic deformation is slip due to dislocations motion. The initial processes of the plastic deformation of the materials during nanoindentation testing can be studied at the atomic level using Molecular Dynamics simulations. Therefore, Molecular Dynamics simulations were performed to determine the corresponding quantitative stress level necessary to trigger dislocation nucleation and activation of the plastic deformation.

Such analysis offers a genuine insight into the processes occurring in the irradiated materials subjected to the indentation process. The hardening modulus is coupled with radiation induced porosity

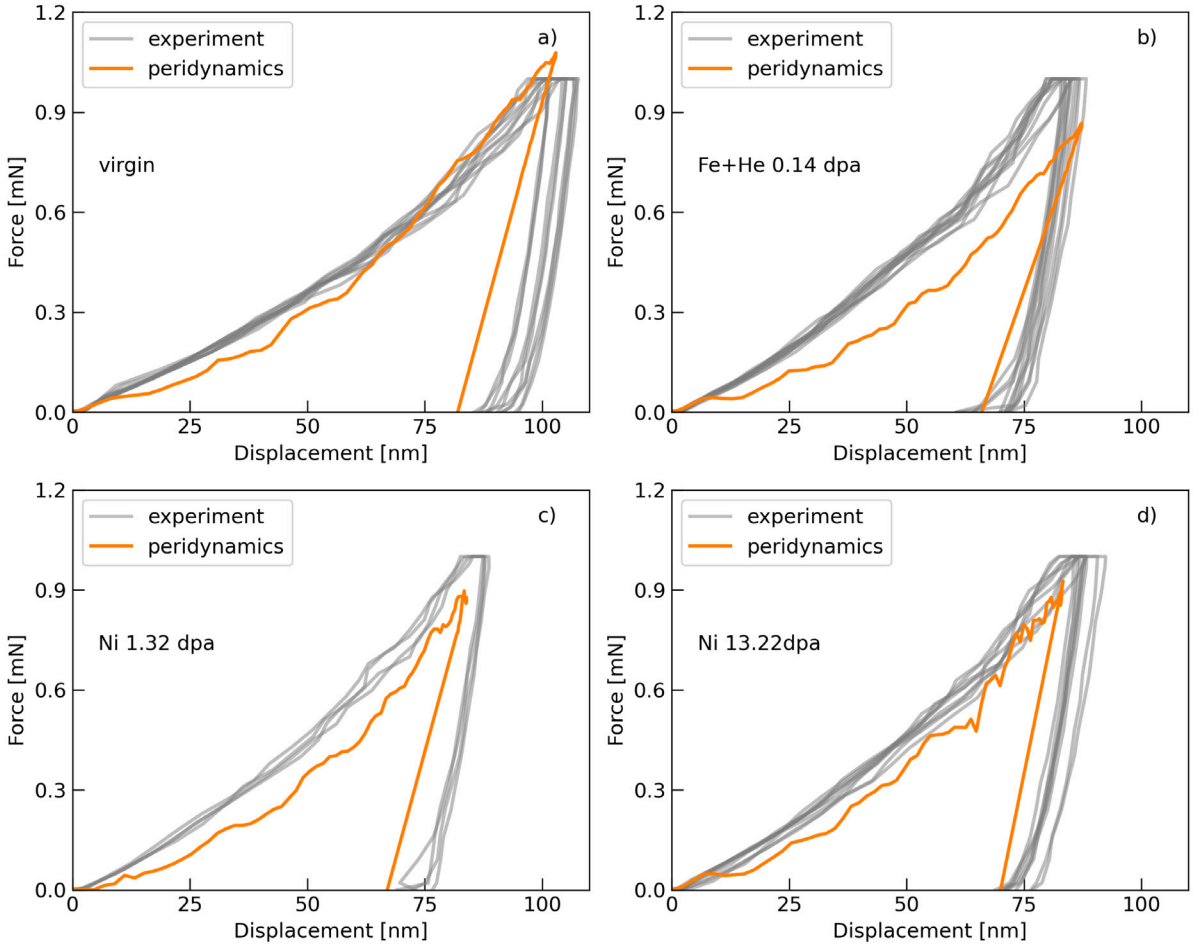

Fig. 16. Comparison of the load–indentation depth curves between the experimental results and the numerical simulations for (a) virgin material and (b–d) different values of dpa.

(Eq. (37)). Moreover, the initial yield point is a function of the irradiation level, expressed by dpa parameter (Eq. (38)). With an increasing dose of radiation, the material's initial yield and stiffness increase. Consequently, larger forces have to be applied to achieve the material's plastic behaviour. As expected, the greatest stress values are located in the vicinity of the indenter tip. With increasing dpa, the stress level also increases causing the growth of porosity. The evolution of porosity, equivalent plastic stretch and HMH equivalent stress under the loads caused by nano-indentation are presented in Fig. 18. The equivalent plastic stretch increases rapidly for the unirradiated material. The radiation induced porosity expressed as a function of dpa significantly affects the process of evolution of plastic stretch in the material. With increasing irradiation dose the rate of equivalent plastic stretch decreases, and, it remains steady during the unloading process. As shown, the highest value of HMH equivalent stress is recorded for the maximum value of the irradiation porosity and indicates the tendency to saturation. This analysis confirmed, that the evolution of porosity results in structural changes.

In Fig. 19, the relationships between the void growth rate and the equivalent plastic stretch are plotted. The evolution of radiation induced porosity is computed directly from the Gurson kinetics law (Eq. (29)), which does not correctly reflect the compressive processes. Gurson's model assumes that the initial porosity level will be substantially reduced due to the indentation process. This is due to the phenomenological assumptions about the fundamental qualities, that the micro-porosity has to close up ahead of the indenter under compressive stress. In the proposed peridynamic pressure-dependent constitutive model the modification of Gurson kinetics is introduced. The increase of initial porosity is generated independently of the pressure direction.

The character of nano/micro porosity evolution is certainly one of the interesting features. The porosity cannot be reduced since material cohesion restoration is impossible. On the contrary, the closed voids are converted to some sort of micro-cracks (of rounded edges), that might become origin of a macro-crack when the continuum is overloaded. The change of the load direction will cause swiftly opening of the micro-cracks and subsequently their evolution. Moreover, the porosity is constantly evolving and might become the origin of a macro-crack when the continuum is overloaded. The main features of the proposed peridynamic elasto-plastic damage model for ion-irradiated materials (Eqs. (40)) are as follows:

- The proposed constitutive model is formulated within the framework of peridynamics theory, where the plastic behaviour of the irradiated materials can be analysed at the nano/micro scale level.
- Radiation-induced defects are described by the porosity parameter reflecting randomly distributed spherical clusters of voids resulting from elastic interactions of energetic particles with lattice atoms.
- Peridynamic porosity is defined as a volume of discontinuities created in the volume of peridynamic particles. The peridynamic porosity can be easily recalculated to damage parameter within Continuum Damage Mechanics (CDM).
- The evolution of radiation induced porosity is driven by the volumetric plastic stretch rate combined with type GTN yield surface.

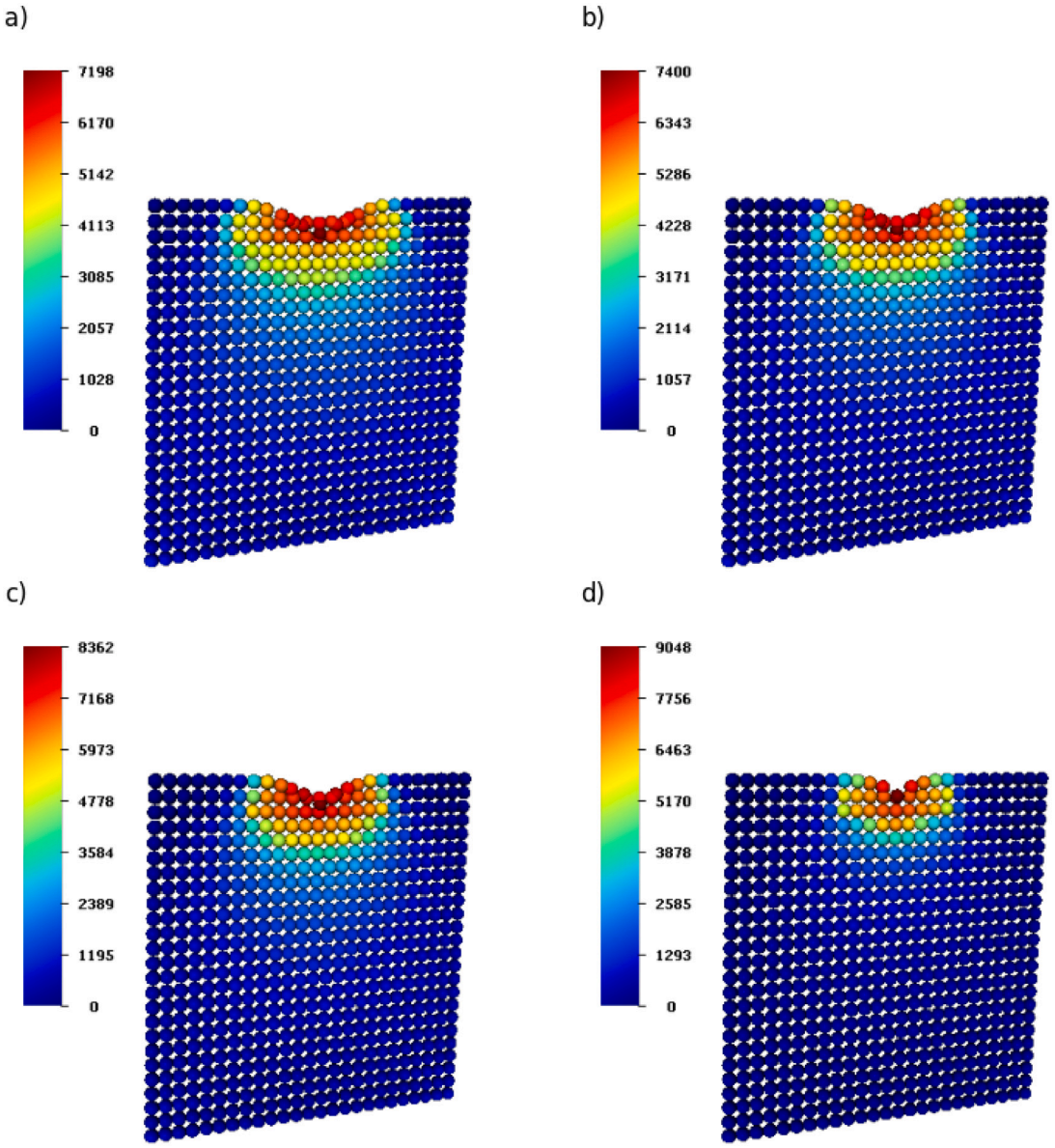

Fig. 17. Distribution of equivalent HMH stress $q_{(k)}$ at maximum indentation depth for several levels of dpa for (a) unirr (b) irr1, (c) irr2 and (d) irr3. The units of stress is MPa.

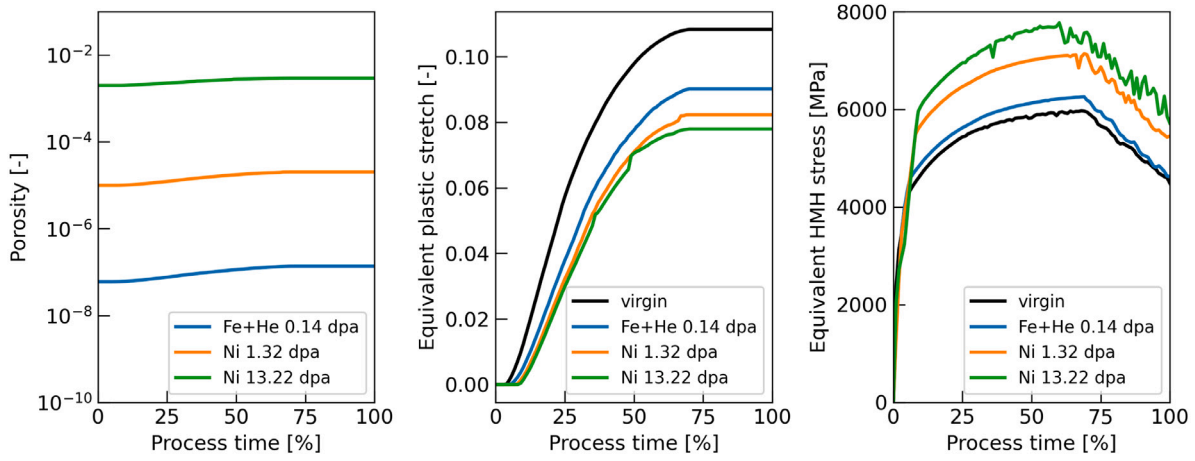

Fig. 18. Development of porosity, equivalent plastic stretch and equivalent HMH stress during nano-indentation processes for different level of initial dpa.

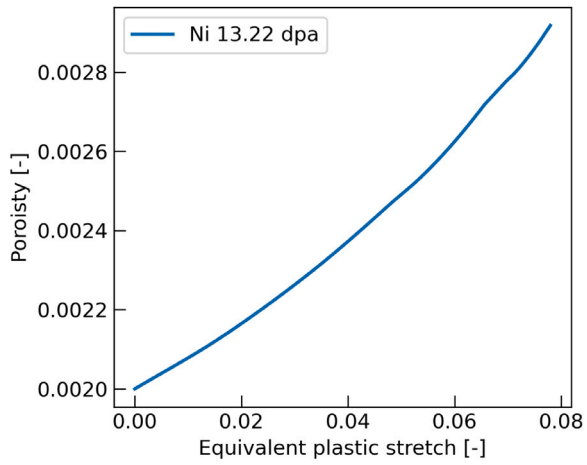

Fig. 19. Evolution of radiation induced porosity as a function of equivalent plastic stretch.

Peridynamic porosity evolution is the progressive physical process that leads to the growth of voids in the volume of peridynamics particles.

- The criterion of failure is formulated based on the critical value of the porosity parameter. The porosity evolution leads to the weakening of the bonds due to the reduction of particle volume. Consequently, an increase of porosity leads to the accumulation and local concentration of internal forces in the neighbourhood of defected volume.
- Gurson–Tvergaard–Needleman (GTN) yield criterion formulated for a porous solid is adopted. GTN model provides the coupling of the radiation induced porosity parameter with the yield function.
- The constitutive relations for irradiation hardening based on the dilatational part of elastic strain energy are formulated. Formulated hardening and softening laws for irradiated materials are based on the physical mechanisms of the dislocation motion impeded by irradiation-induced defects, the annihilation of dislocations, and the unpinning dislocations. The nonlinear irradiation hardening and softening are coupled with the porosity variation. The hardening and softening rules control the evolution of the yield function.

5. Conclusions

The original peridynamic pressure-dependent constitutive model able to predict the porosity evolution for ion-irradiated ductile material is proposed. The new nonlinear relations of the irradiation hardening are introduced into the constitutive relations of the material. The hardening law for irradiated steels accounts for the mechanism of the dislocation motion impeded by irradiation-induced defects, the annihilation of dislocations, and the unpinning dislocations. The combined effects, the irradiation hardening phenomena and the evolution of radiation induced porosity are investigated. To cover the presence of radiation-induced voids in the constitutive model, the volumetric damage is defined at the level of the peridynamic particle. The evolution of the damage parameter is governed by kinetic law expressed in the form of the rate of plastic stretch. The Gurson–Tvergaard–Needleman (GTN) yield criteria expressed in terms of peridynamic variables in order to describe plastic yielding is used. Generally, the constitutive expressions for the yield function, the plastic flow rule, kinetic law of damage evolution and irradiation hardening are expressed in terms of the basic peridynamic variables. Ion irradiations have been carried out using the broad ions fluence range to obtain materials with a wide range of damage level. The defects induced by ion irradiation in the austenitic stainless steel have been investigated by using the nano-indentation technique. Numerical simulations using well-calibrated constitutive models present the characterization of ductile porosity in the ion irradiated material subjected to plastic deformation during indentation tests. The peridynamics constitutive model based on the equation of motion, the integral equation without spatial derivatives, is valid, especially for materials with discontinuities like nano/micro voids, nano/micro inclusions and cracks. Due to this reason, the developed peridynamic model gives a better description of the irradiated components subjected to mechanical loads than models developed in the framework of CDM. Moreover, one of the major drawbacks of the Gurson model is the reduction of porosity due to the compressive process. The voids evolve and might become converted to some sort of micro-cracks when the continuum is overloaded. In the proposed peridynamic model, this problem is corrected.

Finally, several new elements contained in the present paper can be summarized in the following way:

- formulation of the constitutive model with radiation induced damage evolution within the framework of peridynamics theory (PD), from consideration of the physical mechanisms that are involved in plastic flow processes
- defining peridynamic porosity as a new damage variable in peridynamics theory
- proposing new mathematical relation between the radiation damage measure (dpa) and the peridynamic porosity parameter
- defining irradiation hardening controlled by irradiation induced defects
- developing the numerical code using the C programming language based on the mathematical framework of the constitutive relations
- carrying out two experimental campaigns dedicated to irradiated materials: ion irradiation in a wide range of damage levels and nanoindentation tests made on irradiated specimens
- verification of the applicability of GTN yield function expressed in terms of peridynamic variables to analysis the plastic behaviour of the irradiated materials
- simulating the deformation process of the ion irradiated materials numerically during the nanoindentation test employing the peridynamic elasto-plastic damage model

CRediT authorship contribution statement

M. Nowak: Conceptualization, Methodology, Software, Visualization, Writing – original draft, Writing – review & editing. **K. Mulewska:** Methodology, Data curation, Visualization. **A. Azarov:** Methodology, Data curation. **Ł. Kurpaska:** Methodology, Data curation, Writing – review & editing. **A. Ustrzycka:** Conceptualization, Methodology, Visualization, Writing – original draft, Writing – review & editing.

Data availability

No data was used for the research described in the article.

Acknowledgements

This work is supported by the National Science Centre, Poland through the Grant No UMO-2020/38/E/ST8/00453. The Research Council of Norway is acknowledged for the support to the Norwegian Micro- and Nano-Fabrication Facility, NorFab, Poland, project number 295864.

Appendix

The numerical integration of the constitutive Eqs. (40) is based on radial return mapping algorithm for pressure-dependent material model presented by Aravas [58]. The proposed numerical algorithm has been modified in order to adapt it to the new peridynamics model. In the first step of the algorithm, the trial elastic stretch $s^{et}_{(k)(j)}$ is computed assuming that the total stretch increment $\Delta s_{(k)(j)}$ is elastic

$$s^{et}_{(k)(j)} = s^{e[n]}_{(k)(j)} + \Delta s_{(k)(j)} \tag{43}$$

where $s^{e[n]}_{(k)(j)}$ is the known elastic stretch from the previous time step Next, using Eq. (5), the trail elastic dilatation is calculated as

$$\theta^{et}_{(k)} = d\delta \sum_{i=1}^{N} (s^{et}_{(k)(j)})^2 |\mathbf{x}_{(j)} - \mathbf{x}_{(k)}| V_{(j)} \tag{44}$$

Based on the above Eqs. (43), (44), the distortional and dilatation part of the elastic energy are determined using Eqs. (9) and (10) as

$$W^{\kappa t}_{(k)} = a_\kappa (\theta^{et}_{(k)})^2 \quad W^{\mu t}_{(k)} = b \sum_{j=1}^{N} \delta (s^{et}_{(k)(j)})^2 |\mathbf{x}_{(j)} - \mathbf{x}_{(k)}| V_{(j)} - a_\mu (\theta^{et}_{(k)})^2 \tag{45}$$

Finally, the trial hydrostatic pressure $p^t_{(k)}$ and the trial equivalent HMH stress $q^t_{(k)}$ are calculated using Eq. (45)

$$q^t_{(k)} = \sqrt{6\mu W^{\mu t}_{(k)}}, \quad p^t_{(k)} = \sqrt{2\kappa a_\kappa}\,\theta^{et}_{(k)} \tag{46}$$

Substituting Eq. (46) into the yield condition (Eq. (16)) one obtains

$$F^t_{(k)} = \left(\frac{q^t_{(k)}}{\sigma^y_{(k)}} \right)^2 + 2q_1 f \cosh\left(\frac{3q_2 p^t_{(k)}}{2\sigma^y_{(k)}} \right) - (1 + q_3 f^2) \tag{47}$$

If the yield condition is not reached $F^t_{(k)} < 0$, the current step is considered to be elastic. Otherwise, the force density vector is calculated according to Eq. (11) and the numerical procedure is finished. In the case of the plastic step, an iterative method to obtain a plastic correction is needed.

Splitting the increment of total stretch into elastic and plastic part,

$$\Delta s_{(k)(j)} = \Delta s^e_{(k)(j)} + \Delta s^p_{(k)(j)} \tag{48}$$

and similarly, the total increment of dilatation,

$$\Delta\theta_{(k)} = \Delta\theta^e_{(k)} + \Delta\theta^p_{(k)} \tag{49}$$

the trial force density based on Hooke's law is obtained as

$$t_{(k)(j)} = t^{et}_{(k)(j)} - \left[(a_\kappa - a_\mu) 2\delta d \frac{\Lambda_{(k)(j)}}{|\mathbf{x}_{(j)} - \mathbf{x}_{(k)}|} \Delta\theta^p_{(k)} + 2\delta b \Delta s^p_{(k)(j)} \right] \tag{50}$$

Eq. (50) can be split into two orthogonal state expressed in the following form

$$t^{\mu}_{(k)(j)} = t^{et\mu}_{(k)(j)} + a_\mu 2\delta d \frac{\Lambda_{(k)(j)}}{|\mathbf{x}_{(j)} - \mathbf{x}_{(k)}|} \Delta\theta^p_{(k)} - 2\delta b \Delta s^p_{(k)(j)} \tag{51}$$

$$t^{\kappa}_{(k)(j)} = t^{et\kappa}_{(k)(j)} - a_\kappa 2\delta d \frac{\Lambda_{(k)(j)}}{|\mathbf{x}_{(j)} - \mathbf{x}_{(k)}|} \Delta\theta^p_{(k)} \tag{52}$$

The incremental plastic dilatation $\Delta\theta^p_{(k)}$ can be written using Eq. (5) as

$$\Delta\theta^p_{(k)} = d\delta \sum_{i=1}^{N} \Delta s^p_{(k)(j)} \Lambda_{(k)(j)} V_{(j)} \tag{53}$$

Eq. (52) can be simplified by substituting Eq. (13)

$$\theta_{(k)} = \theta^{et}_{(k)} - \Delta\theta^p_{(k)} \tag{54}$$

The incremental plastic dilatation can be rewritten by substituting Eq. (25) into Eq. (53)

$$\Delta\theta^p_{(k)} = d\delta \sum_{j=1}^{N} \frac{1}{V_{(j)}} \left[\Delta s^{pp}_{(k)} \frac{\partial p_{(k)}}{\partial t_{(k)(j)}} + \Delta s^{pq}_{(k)} \frac{\partial q_{(k)}}{\partial t_{(k)(j)}} \right] \Lambda_{(k)(j)} V_{(j)} \tag{55}$$

After some algebraic manipulation and noting that plastic dilatation is not dependent on distortion state, Eq. (55) can be expressed as

$$\Delta\theta^p_{(k)} = d\delta \Delta s^{pp}_{(k)} \sum_{j=1}^{N} \frac{\partial p_{(k)}}{\partial t_{(k)(j)}} \Lambda_{(k)(j)} \tag{56}$$

Having all variables dependent on the two unknowns $\Delta s^{pp}_{(k)}$ and $\Delta s^{pq}_{(k)}$, the system of nonlinear equations (40) is solved using Newton method. The main steps of this method are shown below. In the first step the initial values of unknown variables are assumed to be equal zero

$$\Delta s^{pp}_{(k)} = 0, \qquad \Delta s^{pq}_{(k)} = 0 \tag{57}$$

Next the values of pressure, equivalent HMH stress and dilatation are calculated from the trial state

$$p_{(k)} = p^t_{(k)}, \quad q_{(k)} = q^t_{(k)}, \quad \theta_{(k)} = \theta^t_{(k)} \tag{58}$$

The derivative of the equivalent HMH stress with respect to the force density vector is computed as

$$\frac{\partial q_{(k)}}{\partial t_{(k)(j)}} = \frac{\partial q_{(k)}}{\partial t^{\mu}_{(k)(j)}} = \frac{\partial q_{(k)}}{\partial W^{\mu}_{(k)}} \frac{\partial W^{\mu}_{(k)}}{\partial t^{\mu}_{(k)(j)}} \tag{59}$$

where

$$\frac{\partial q_{(k)}}{\partial W^{\mu}_{(k)}} = \frac{6\mu}{2\sqrt{6\mu W^{\mu}_{(k)}}} \tag{60}$$

and

$$\frac{\partial W^{\mu}_{(k)}}{\partial t^{\mu}_{(k)(j)}} = \left[\frac{1}{2\delta b} |\mathbf{x}_{(j)} - \mathbf{x}_{(k)}| t_{(k)(j)} + \frac{d}{b} a_\mu \left(1 - \frac{a_\kappa}{a_\mu} \right) \Lambda_{(k)(j)} \theta_{(k)} \right] V_{(j)} \tag{61}$$

Following the approach presented by Aravas [58], it is assumed that the derivative of the equivalent HMH stress with respect to the force density vector is equal to the same derivatives taken form trial state

$$\frac{\partial q_{(k)}}{\partial t_{(k)(j)}} = \frac{\partial q^t_{(k)}}{\partial t^t_{(k)(j)}} \tag{62}$$

Next, the derivative of the pressure with respect to the force density vector is calculated

$$\frac{\partial p_{(k)}}{\partial t_{(k)(j)}} = \frac{\partial p_{(k)}}{\partial t^{\kappa}_{(k)(j)}} = \sqrt{2\kappa a_\kappa} \frac{|\mathbf{x}_{(j)} - \mathbf{x}_{(k)}|}{2\delta a_\kappa d \Lambda_{(k)(j)}} \tag{63}$$

The above expression is computed outside the Newton iteration loop because it is independent on the unknown variables. The following derivative has to be calculated inside the Newton loop.

$$\frac{\partial F_{(k)}}{\partial p_{(k)}} = 2q_1 f_{(k)} \sinh\left(\frac{3q_2 p_{(k)}}{2\sigma^y_{(k)}} \right) \frac{3q_2}{2\sigma^y_{(k)}} \tag{64}$$

and

$$\frac{\partial F_{(k)}}{\partial q_{(k)}} = \frac{2q_{(k)}}{(\sigma^y_{(k)})^2} \tag{65}$$

Finally, the values of two non-linear equations are computed

$$\phi_1 = \Delta s^{pp}_{(k)} \frac{\partial F_{(k)}}{\partial q_{(k)}} - \Delta s^{pq}_{(k)} \frac{\partial F_{(k)}}{\partial p_{(k)}} \tag{66}$$

and

$$\phi_2 = F_{(k)}(\Delta s^{pp}_{(k)}, \Delta s^{pq}_{(k)}) \tag{67}$$

If the values of two above equations are close to zero, then the Newton iteration loop is finished. Otherwise, the Jacobian matrix $\mathbf{J}$ is calculated and the increment of unknown variables can be obtained using matrix notation

$$\Delta\mathbf{d} = \mathbf{J}^{-1}\mathbf{F} \tag{68}$$

where

$$\mathbf{J}=\begin{bmatrix}\frac{\partial\phi_1}{\partial\Delta s^{pp}_{(k)}} & \frac{\partial\phi_1}{\partial\Delta s^{pq}_{(k)}}\\ \frac{\partial\phi_2}{\partial\Delta s^{pp}_{(k)}} & \frac{\partial\phi_2}{\partial\Delta s^{pq}_{(k)}}\end{bmatrix},\quad \mathbf{F}=\begin{bmatrix}-\phi_1(\Delta s^{pp}_{(k)},\Delta s^{pq}_{(k)})\\ -\phi_2(\Delta s^{pp}_{(k)},\Delta s^{pq}_{(k)})\end{bmatrix},\quad \Delta\mathbf{d}=\begin{bmatrix}d\Delta s^{pp}_{(k)}\\ d\Delta s^{pq}_{(k)}\end{bmatrix} \tag{69}$$

Finally the value of the new increment of the unknowns variables is calculated using the following form

$$\mathbf{d}^{n+1}=\mathbf{d}^{n}+\Delta\mathbf{d}. \tag{70}$$

If the norm of vector $\mathbf{F}$ is close to the assumed tolerance, the Newton method is finished and the obtained values are used to evaluate the force vector state. In order to calculate the Jacobian matrix the following derivatives with respect to unknowns variables have to be determined

$$\frac{\partial\phi_1}{\partial\Delta s^{pp}_{(k)}}=\frac{\partial F_{(k)}}{\partial q_{(k)}}-\Delta s^{pq}_{(k)}\frac{\partial^2 F_{(k)}}{\partial p^2_{(k)}}\frac{\partial p_k}{\partial\Delta s^{pp}_{(k)}} \tag{71}$$

$$\frac{\partial\phi_1}{\partial\Delta s^{pq}_{(k)}}=\Delta s^{pp}_{(k)}\frac{\partial^2 F_{(k)}}{\partial q^2_{(k)}}\frac{\partial q_k}{\partial\Delta s^{pq}_{(k)}}-\frac{\partial F_{(k)}}{\partial p_{(k)}} \tag{72}$$

$$\frac{\partial\phi_2}{\partial\Delta s^{pp}_{(k)}}=\frac{\partial F_{(k)}}{\partial p_{(k)}}\frac{\partial p_{(k)}}{\partial\Delta s^{pp}_{(k)}} \tag{73}$$

$$\frac{\partial\phi_2}{\partial\Delta s^{pq}_{(k)}}=\frac{\partial F_{(k)}}{\partial q_{(k)}}\frac{\partial q_{(k)}}{\partial\Delta s^{pq}_{(k)}} \tag{74}$$

where

$$\frac{\partial^2 F_{(k)}}{\partial p^2_{(k)}}=2q_1 f_{(k)}\cosh\left(\frac{3q_2 p_{(k)}}{2\sigma^{y}_{(k)}}\right)\left(\frac{3q_2}{2\sigma^{y}_{(k)}}\right)^2 \tag{75}$$

$$\frac{\partial^2 F_{(k)}}{\partial q^2_{(k)}}=\frac{2}{(\sigma^{y}_{(k)})^2} \tag{76}$$

$$\begin{aligned}\frac{\partial q_{(k)}}{\partial\Delta s^{pq}_{(k)}}&=\frac{\partial q_{(k)}}{\partial t^{\mu}_{(k)(j)}}\frac{\partial t^{\mu}_{(k)(j)}}{\partial\Delta s^{p}_{(k)(j)}}\frac{\partial\Delta s^{p}_{(k)(j)}}{\partial\Delta s^{pq}_{(k)}}\\ \frac{\partial p_{(k)}}{\partial\Delta s^{pp}_{(k)}}&=\frac{\partial p_{(k)}}{\partial t^{\kappa}_{(k)(j)}}\frac{\partial t^{\kappa}_{(k)(j)}}{\partial\Delta\theta^{p}_{(k)}}\frac{\partial\theta^{p}_{(k)}}{\partial\Delta s^{p}_{(k)(j)}}\frac{\partial\Delta s^{p}_{(k)(j)}}{\partial\Delta s^{pp}_{(k)}}\end{aligned} \tag{77}$$

$$\frac{\partial t^{\mu}_{(k)(j)}}{\partial\Delta s^{p}_{(k)(j)}}=-2\delta b \tag{78}$$

$$\frac{\partial t^{\kappa}_{(k)(j)}}{\partial\Delta\theta^{p}_{(k)}}=-a_{\kappa}2\delta d\frac{\Lambda_{(k)(j)}}{|\mathbf{x}_{(j)}-\mathbf{x}_{(k)}|} \tag{79}$$

$$\frac{\partial\Delta s^{p}_{(k)(j)}}{\partial\Delta s^{pp}_{(k)}}=\frac{1}{V_{(j)}}\frac{\partial p_{(k)}}{\partial t_{(k)(j)}} \tag{80}$$

$$\frac{\partial\Delta s^{p}_{(k)(j)}}{\partial\Delta s^{pq}_{(k)}}=\frac{1}{V_{(j)}}\frac{\partial q_{(k)}}{\partial t_{(k)(j)}} \tag{81}$$

$$\frac{\partial\theta^{p}_{(k)}}{\partial\Delta s^{p}_{(k)(j)}}=d\delta\Lambda_{(k)(j)}V_{(j)} \tag{82}$$

References

[1] Barton N, Arsenlis A, Marian J. MA polycrystal plasticity model of strain localization in irradiated iron. J Mech Phys Solids 2013;61:341–51.

[2] Skoczeń B, Ustrzycka A. Kinetics of evolution of radiation induced microdamage in ductile materials subjected to time-dependent stresses. Int J Plast 2016;80:86–110.

[3] Hure J, Shawish S, Cizelj L, Tanguy B. Intergranular stress distributions in polycrystalline aggregates of irradiated stainless steel. J Nucl Mater 2017;492:157–70.

[4] Zhou T, Zhao F, Zhou H, Zhang F, Wang P. Atomistic simulation and continuum modeling of the dynamic tensile fracture and damage evolution of solid single crystalline Al with He bubble. Int J Mech Sci 2022;234:107681.

[5] Chen Y, Liu Y, Fang Q, Li J, Liu Y, Liaw PK. An unified model for dislocations interacting with complex-shape voids in irradiated metals. Int J Mech Sci 2020;185:105689.

[6] Xiao X, Li S, Yu L. Effect of irradiation damage and indenter radius on pop-in and indentation stress-strain relations: Crystal plasticity finite element simulation. Int J Mech Sci 2021;199:106430.

[7] Wu W-D, Shao J-L. Numerical and theoretical study on shock-induced coalescence of He bubbles. Int J Mech Sci 2022;234:107699.

[8] Kachanov L. On the kinetics of crack growth. J Appl Math Mech 1961;25(3):739–45.

[9] Murakami S. Notion of continuum damage mechanics and its application to anisotropic creep damage theory. J Eng Mater Technol 1984;105:99–105.

[10] Chaboche J. Continuum damage mechanics: Part II – damage growth, crack initiation, and crack growth. J Appl Mech 1988;55:65–72.

[11] Chaboche J. Continuum damage mechanics: Part I – general concepts. J Appl Mech 1988;55:59–64.

[12] Szuwalski K, Ustrzycka A. Optimal design of bars under nonuniform tension with respect to mixed creep rupture time. Int J Non-Linear Mech 2012;47:55–60.

[13] Szuwalski K, Ustrzycka A. The influence of boundary conditions on optimal shape of annular disk with respect to ductile creep rupture time. Eur J Mech A Solids 2013;37:79–85.

[14] Gurson A. Continuum theory of ductile rupture by void nucleation and growth. Part I. Yield criteria and flow rules for porous ductile media. J Eng Mater Technol 1975.

[15] Tvergaard V, Needleman A. Analysis of the cup-cone fracture in a round tensile bar. Acta Metall 1984;32(1):157–69.

[16] Gurson A. A continuous damage mechanics model for ductile fracture. J Eng Mater Technol 1977;107:83–9.

[17] Gholipour H, Biglari F, Nikbin K. Experimental and numerical investigation of ductile fracture using gtn damage model on in-situ tensile tests. Int J Mech Sci 2019;164:105170.

[18] Nasir MW, Chalal H, Abed-Meraim F. Formability prediction using bifurcation criteria and GTN damage model. Int J Mech Sci 2021;191:106083.

[19] Wu H, Xu W, Shan D, Jin BC. Mechanism of increasing spinnability by multi-pass spinning forming – Analysis of damage evolution using a modified GTN model. Int J Mech Sci 2019;159:1–19.

[20] Silling S. Reformulation of elasticity theory for discontinuities and long-range forces. J Mech Phys Solids 2000;48(1):175–209.

[21] Silling S, Askari E. A meshfree method based on the peridynamic model of solid mechanics. Comput Struct 2005;83(17):1526–35, Advances in Meshfree Methods.

[22] Agwai A, Guven I, Madenci E. Crack propagation in multilayer thin-film structures of electronic packages using the peridynamic theory. Microelectron Reliab 2011;51(12):2298–305.

[23] Liu S, Fang G, Fu M, Yan X, Meng S, Liang J. A coupling model of element-based peridynamics and finite element method for elastic-plastic deformation and fracture analysis. Int J Mech Sci 2022;220:107170.

[24] Friedrich LF, Colpo AB, Kosteski LE, Vantadori S, Iturrioz I. A novel peridynamic approach for fracture analysis of quasi-brittle materials. Int J Mech Sci 2022;227:107445.

[25] Tian D-L, Zhou X-P. A continuum-kinematics-inspired peridynamic model of anisotropic continua: Elasticity, damage, and fracture. Int J Mech Sci 2021;199:106413.

[26] Zhao T, Shen Y. A nonlocal model for dislocations with embedded discontinuity peridynamics. Int J Mech Sci 2021;197:106301.

[27] Scherer J-M, Besson J, Forest S, Hure J, Tanguy B. A strain gradient plasticity model of porous single crystal ductile fracture. J Mech Phys Solids 2021;156:104606.

[28] Petryk H, Stupkiewicz S. A minimal gradient-enhancement of the classical continuum theory of crystal plasticity. Part I: The hardening law. Arch Mech 2016;68:459–85.

[29] Stupkiewicz S, Petryk H. A minimal gradient-enhancement of the classical continuum theory of crystal plasticity. Part II: Size effects. Arch Mech 2016;68:487–513.

[30] Tůma K, Stupkiewicz S, Petryk H. Phase-field study of size-dependent morphology of austenite–twinned martensite interface in CuAlNi. J Mech Phys Solids 2016;95:284–307.

[31] Sumelka W, Nowak M. On a general numerical scheme for the fractional plastic flow rule. Mech Mater 2018;116:120–9, IUTAM Symposium on Dynamic Instabilities in Solids.

[32] Szymczyk M, Nowak M, Sumelka W. Plastic strain localization in an extreme dynamic tension test of steel sheet in the framework of fractional viscoplasticity. Thin-Walled Struct 2020;149:106522.

[33] Crété J, Longère P, Cadou J. Numerical modelling of crack propagation in ductile materials combining the GTN model and X-FEM. Comput Methods Appl Mech Engrg 2014;275:204–33.

[34] Zhao J, Tang H, Xue S. Peridynamics versus XFEM: a comparative study for quasi-static crack problems. Front. Struct. Civ. Eng. 2017;12:548–57.

[35] Ongaro G, Bertani R, Galvanetto U, Pontefisso A, Zaccariotto M. A multiscale peridynamic framework for modelling mechanical properties of polymer-based nanocomposites. Eng Fract Mech 2022;274:108751.

[36] Madenci E, Oterkus S. Ordinary state-based peridynamics for plastic deformation according to von mises yield criteria with isotropic hardening. J Mech Phys Solids 2016;86:192–219.
[37] Pashazad H, Kharazi M. A peridynamic plastic model based on von mises criteria with isotropic, kinematic and mixed hardenings under cyclic loading. Int J Mech Sci 2019;156:182–204.
[38] Silling SA, Epton M, Weckner O, Xu J, Askari E. Peridynamic states and constitutive modeling. J Elasticity 2007;88:151–84.
[39] Tupek M, Rimoli J, Radovitzky R. An approach for incorporating classical continuum damage models in state-based peridynamics. Comput Methods Appl Mech Engrg 2013;263:20–6.
[40] Hu Y, Feng G, Li S, Sheng W, Zhang C. Numerical modelling of ductile fracture in steel plates with non-ordinary state-based peridynamics. Eng Fract Mech 2020;225:106446.
[41] Silling S. Stability of peridynamic correspondence material models and their particle discretizations. Comput Methods Appl Mech Engrg 2017;322:42–57.
[42] Ustrzycka A, Mróz Z, Kowalewski Z, Kucharski S. Analysis of fatigue crack initiation in cyclic microplasticity regime. Int J Fatigue 2020;131:105342.
[43] Nahshon K, Hutchinson J. Modification of the Gurson model for shear failure. Eur J Mech A Solids 2008;27(1):1–17.
[44] Madou K, Leblond J-B. A Gurson-type criterion for porous ductile solids containing arbitrary ellipsoidal voids—I: Limit-analysis of some representative cell. J Mech Phys Solids 2012;60(5):1020–36.
[45] Ustrzycka A, Skoczen B, Nowak M, Kurpaska L, Wyszkowska E, Jagielski J. Elastic–plastic-damage model of nano-indentation of the ion-irradiated 6061 aluminium alloy. Int J Damage Mech 2020;29:1271–305.
[46] Sencer B, Kennedy JR, Cole J, Maloy S, Garner F. Microstructural analysis of an HT9 fuel assembly duct irradiated in FFTF to 155 dpa at 443. J Nucl Mater 2009;393:235–41.
[47] Porollo S, Vorobjev AN, Konobeev YV, Dvoriashin AM, Krigan VM, Budylkin NI, Mironova EG, Garner FA. Swelling and void-induced embrittlement of austenitic stainless steel irradiated to 73–82 dpa at 335–360 °C. J Nucl Mater 1998;258–263:1613–7.
[48] Courcelle A, Bisor C, Piozin E, Kountchou M, Gavoille P, Flem M, Séran J-L. Evolution under irradiation of optimized austenitic steel for gen-iv reactors. Impact on fuel cladding properties and performances. In: MINOS 2nd international workshop, irradiation of nuclear materials: flux and dose effects, Vol. 115. 2016, (04003).
[49] Nordlund K, Zinkle SJ, Sand AE, Granberg F, Averback RS, Stoller R, Suzudo T, Malerba L, Banhart F, Weber WJ, Willaime F, Dudarev SL, Simeone D. Primary radiation damage: A review of current understanding and models. J Nucl Mater 2018;512:450–79.
[50] Ling C, Tanguy B, Besson J, Forest S, Latourte F. Void growth and coalescence in triaxial stress fields in irradiated FCC single crystals. J Nucl Mater 2017;492:157–70.
[51] Byun T, Farrell K, Lee E, Mansur L, Maloy S, James M, Johnson W. Temperature effects on the mechanical properties of candidate SNS target container materials after proton and neutron irradiation. J Nucl Mater 2002;303:34–43.
[52] Kocks U, Mecking H. Physics and phenomenology of strain hardening: the FCC case. Prog Mater Sci 2003;48:171–273.
[53] Byun T, Farrell K, Lee E, Hunn J, Mansur L. Strain hardening and plastic instability properties of austenitic stainless steels after proton and neutron irradiation. J Nucl Mater 2001;298:269–79.
[54] Osetsky Y, Stoller R, Matsukawa Y. Dislocation–stacking fault tetrahedron interaction: what can we learn from atomic-scale modelling. J Nucl Mater 2004;329–333:1228–32.
[55] Lehtinen A, Granberg F, Laurson L, Nordlund K, Alava M. Multiscale modeling of dislocation-precipitate interactions in Fe: From molecular dynamics to discrete dislocations. J Nucl Mater 2016;93:013309.
[56] Chen L, Liu W, Yu L, Cheng Y, Ren K, Sui H, Yi X, Duan H. Probabilistic and constitutive models for ductile-to-brittle transition in steels: A competition between cleavage and ductile fracture. J Mech Phys Solids 2020;135:103809.
[57] Ziegler JF, Ziegler M, Biersack J. SRIM – the stopping and range of ions in matter (2010). Nucl Instrum Methods Phys Res B 2010;268:1818–23.
[58] Aravas N. On the numerical integration of a class of pressure-dependent plasticity models. Internat J Numer Methods Engrg 1987;24(7):1395–416.